Research Square

Preprints are preliminary reports that have not undergone peer review.
They should not be considered conclusive, used to inform clinical practice,
or referenced by the media as validated information.

Seismic Performance of the Masonry Infill RC Frame Structure Strengthened with Engineered Cementitious Composite

Subodh Kumar
IIT Kanpur: Indian Institute of Technology Kanpur
Rajat Avasthi
IIT Kanpur: Indian Institute of Technology Kanpur
Durgesh Rai
dcrai@iitk.ac.in

Indian Institute of Technology Kanpur https://orcid.org/0000-0002-8789-2659

Research Article

Keywords: ECC, Masonry, RC frame, Cyclic, In-plane loading, Ground motion, Shake table

Posted Date: June 4th, 2026

DOI: https://doi.org/10.21203/rs.3.rs-9770519/v1

License: This work is licensed under a Creative Commons Attribution 4.0 International License.
Read Full License

Seismic Performance of the Masonry Infill RC Frame Structure Strengthened with Engineered Cementitious Composite

Subodh Kumar [1] (corresponding author), Rajat Avasthi[2], Durgesh C. Rai[3]

Abstract

Masonry infill walls in reinforced concrete (RC) frames are susceptible to horizontal forces in both in-plane and out-of-plane directions during seismic events. These forces can lead to brittle out-of-plane failures due to the loss of flexural strength. Therefore, effective strengthening techniques are required to enhance the seismic performance of masonry structures by improving ductility and energy dissipation. Engineered Cementitious Composites (ECC) offer a promising alternative for strengthening masonry infills due to their strain-hardening behaviour and ability to undergo multiple cracking. This study investigates the seismic performance of masonry infill RC frames strengthened with a single layer of ECC under combined in-plane and out-of-plane loading. A cost-effective ECC using locally sourced polyester fibers was used which were significantly more affordable than the commonly used Polyvinyl Alcohol (PVA) fibers. Despite a lower tensile strength of polyster fibers, this ECC achieved a strain capacity of 1.88% and a strength of 2.17 MPa, which was found sufficient for strengthening masonry walls. Further, the ECC was prepared using readily available materials such as Portland Pozzolana Cement (PPC), river sand, and Fly Ash, significantly reducing manufacturing costs to about one-fifth of standard PVA-based ECCs. An experimental study was conducted on the single bay half-scaled model of the masonry infill RC frame structure strengthened with the ECC layer on one side of the wall. The in-plane loading was applied using a servo-hydraulic actuator, followed by the out-of-plane loading using a unidirectional shaking table. Results indicated that the ECC layer effectively reduced severe cracking in the infill masonry wall, enhancing its in-plane strength by approximately 20% compared to the unstrengthened specimen. The ECC layer effectively prevented severe cracking in the infill, safeguarding the masonry fragments from falling during out-of-plane loading. The ECC layer enhanced the stability of the masonry infill in the out-of-plane direction, ensuring integrity of the infill even as the surrounding frame was damaged. An analytical approach was developed to estimate the in-plane strength of masonry infill in reinforced concrete frames, aiding in the design of wall panels and confining elements. It focuses on shear sliding and diagonal cracking as key failure modes observed in experiments.

Keywords: ECC, Masonry, RC frame, Cyclic, In-plane loading, Ground motion, Shake table

[1] *Former Ph. D. Scholar, Dept. of Civil Engineering, Indian Institute of Technology Kanpur, UP 208016, India, Email: subodh.nits@gmail.com*
[2] *Former Ph. D. Scholar, Dept. of Civil Engineering, Indian Institute of Technology Kanpur, Kanpur, UP 208016, India, Email: ravasthi@iitk.ac.in*
[3] *Professor, Dept. of Civil Engineering, Indian Institute of Technology Kanpur, Kanpur, UP 208016, India, Email: dcrai@iitk.ac.in*

1. INTRODUCTION

Masonry infill walls are extensively used in reinforced concrete (RC) frame structures, particularly in developing countries like India, due to their low cost, local availability, and ease of construction. Though often considered non-structural elements, infill walls significantly influence the global response of RC frames by enhancing lateral stiffness and strength, while the surrounding frame provides confinement that delays disintegration after cracking. This interaction creates a composite system that combines the strength and stiffness of the infill with the ductility of the RC frame. During seismic events, masonry infill walls are subjected to simultaneous in-plane (IP) and out-of-plane (OOP) loading. Prior in-plane damage weakens infills, making them prone to out-of-plane failure during aftershocks, which can cause panel dislodgement and debris fall. This OOP instability, often overlooked in seismic assessments, presents a serious life-safety hazard. Past earthquakes, including the 2001 Bhuj and 2015 Nepal events, revealed the vulnerability of masonry infill walls to such combined actions, with widespread damage and disintegration of panels. The arching mechanism, which typically resists OOP loads, is impaired once the infill sustains significant IP damage, reducing the OOP capacity of the panel. Despite this, the out-of-plane strength of infill walls is often conservatively neglected in seismic design. In India, where over 60% of the land area lies in seismic zones with intensities of VII and above, masonry continues to be the most prevalent construction method. Under IP loading, masonry can fail through various mechanisms such as diagonal tension, diagonal compression, and bed-joint sliding. Such damage critically weakens the infill's OOP resistance and contributes to the poor seismic performance of RC frame-infill systems. Therefore, there is an urgent need for practical and effective retrofitting strategies that enhance the seismic resilience of masonry infill walls under combined loading conditions.

Previous research has explored the application of fiber-reinforced polymers (FRPs), such as bars or strips, bonded externally to masonry surfaces using epoxy adhesives (Tomaževič et al. 2009; Oliveira et al. 2011; Moon et al. 2007). Although FRP systems have proven effective for structural strengthening, challenges such as debonding, high material cost, and poor thermal resistance of epoxy have been widely reported. To address these limitations, systems like textile-reinforced mortar (TRM) and fabric-reinforced cementitious matrix (FRCM) have been developed. These systems employ advanced fiber textiles embedded in inorganic matrices, typically cement-based mortars, providing a more durable and thermally stable strengthening solution (Prota et al. 2006; Papanicolaou 2008; D'Ambrisi et al. 2013; Carozzi et al. 2014; Gattesco et al. 2015; Sagar et al. 2017; Giaretton et al. 2018). In recent years, a promising alternative strengthening approach has involved the use of engineered cementitious composites (ECC) as overlay materials for masonry retrofitting. Engineered cementitious composite (ECC) is a cementitious matrix-based composite that possesses high tensile strain between 2% to 8% (Yu et al. 2017, Zhang et al. 2017), making it a suitable material for seismic strengthening. The effectiveness of ECC in strengthening masonry structures was investigated in the past, and it was found that ECC improved the in-plane and out-of-plane performance of the masonry (Lin et al. 2014; Dehghani et al. 2015). Recent experiments using ECC with moderate tensile strength demonstrated significant gains in compressive and flexural capacity, while also reducing brittle failure in masonry elements (Kumar and Rai 2024). It was evident from the experimental study that the ECC was helpful in preventing the diagonal cracking of the walls, and the failure was converted to rocking mode after the application of the ECC layer (Deng and Yang 2018). The effectiveness of the ECC layer was investigated by performing the shake-table test on a 2/3 scale, 2-bay, and 3-story masonry infilled RC frame (Koutromanos et al., 2013). One bottom-story wall was retrofitted with the ECC layer, and it was found that the ECC was helpful in enhancing the base shear capacity by 70%. The ECC was helpful in avoiding the diagonal cracking of the masonry infill since no visible crack was observed during the test. Previous experimental studies have

demonstrated that ECC greatly enhanced the performance of masonry arches under both static and dynamic loads, effectively preventing collapse (Avasthi et al. 2025). Previous studies have primarily utilized ECC with high-quality fibers, such as Polyethylene (PE) and Polyvinyl Alcohol (PVA), which contribute to approximately 80% of the total manufacturing cost. The limited availability and high cost of these fibers make ECC less economically viable in many regions. As a result, several experimental studies have explored the use of alternative, more affordable fibers to reduce the overall cost of ECC production (Kumar and Rai 2022 and 2023).

The present study investigates the performance of the masonry infill RC frame strengthened with ECC subjected to combined in-plane and out-of-plane loading. The control confined masonry specimen used in the study was adopted from a previously conducted experimental study at IIT Kanpur. During earthquakes, infill walls are subjected to simultaneous in-plane and out-of-plane loading. In-plane damage significantly reduces their out-of-plane strength, compromising stability. To capture this interaction realistically, the present study employed a unique bidirectional loading protocol, combining slow cyclic in-plane drifts with out-of-plane dynamic excitation using shake table–induced ground motions (Komaraneni et al. 2011).

2. MATERIAL AND METHODS

2.1 Specimen details

The half-scaled test specimen had a dimension of 2.7 m×1.7 m, and the thickness of the half-brick thick wall was equal to half of the length of the brick (64 mm). A plaster layer of 6 mm thickness was applied on either side of the masonry infill in the control masonry infill (MIF-CS) wall specimen. The dimensions of the masonry infill test specimens were based on the previous study conducted at IIT Kanpur (Sagar et al. 2019). A strengthened specimen (MIF-EC), identical in size to MIF-CS, was prepared by applying a 6 mm ECC layer on one side of the wall using the trowelling method. The frame columns and beams had a dimension of 125 mm × 200 mm, and the dimension of the masonry infill was 2300 mm × 1300 mm. The overall dimension of the ECC-strengthened masonry infill RC wall (MIF-EC) was 2.5 m x 1.5 m, the same as that of the MIF-CS specimen (Figure 1). In the RC frame, both the beams and columns had the same reinforcement, i.e., four longitudinal bars of 12 mm diameter and stirrups of 6 mm diameter with 100 mm centre-to-centre spacing (Figure 1). The geometric dimensions and the reinforcement details of the MIF-CS and MIF-EC specimens are presented in Figure 1a and Figure 1b, respectively. The half-scaled specimens of the masonry infill frame were constructed in a manner similar to that of the actual practice. The construction process was conducted in a series of defined stages. Initially, the concrete casting of the reinforced concrete (RC) frame was completed. This was followed by the brick-laying phase. In the final stage, a plaster layer was applied to the finished wall of the MIF-CS specimen, while an engineered cementitious composite (ECC) layer was utilized for the front wall of the MIF-EC specimen in place of the plaster.

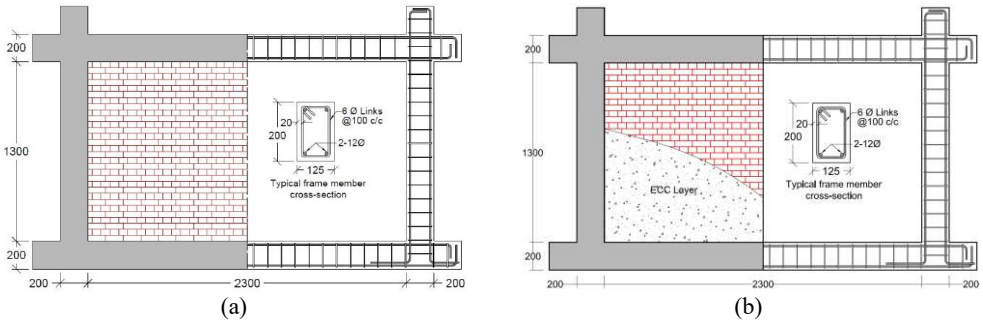


Figure 1. Geometric and sectional properties (a) MIF-CS and (b) MIF-EC wall

In conventional construction practice, the RC frame is erected first, followed by the masonry infill, with the primary load-resisting mechanism governed by the frame. The half-scale masonry infill frame specimens were constructed following this sequence, as shown in Figure 2. Stage I involved casting the RC frame, followed by stepwise masonry construction in Stage II to prevent instability during construction. Stage III concluded with the completion of the brickwork (Figure 2) and subsequent moist curing. In Stage IV, a finishing layer was applied once the masonry attained sufficient strength. For the control specimen (MIF-CS), a conventional plaster layer was used, whereas for the strengthened specimen (MIF-EC), a 6 mm-thick ECC layer was applied on one side of the wall. The construction sequence up to Stage III remained identical for both specimens.

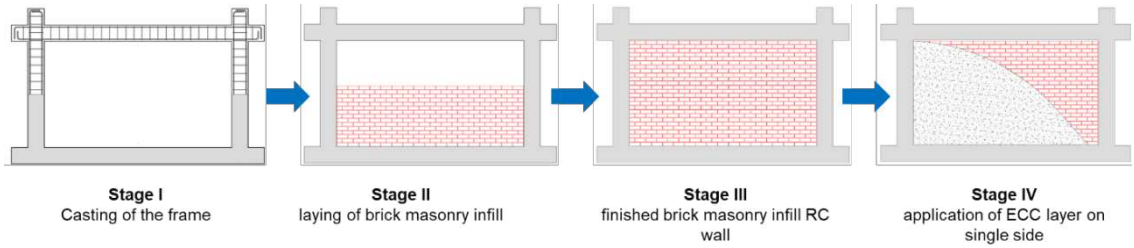


Figure 2. Steps involved in the construction and strengthening of the masonry infill RC wall

The step-by-step procedure for preparing the physical model is illustrated in Figure 3. The frame structure was constructed in a horizontal position, which was later lifted. The main reinforcement and the stirrups were assembled as per the details provided in Figure 1. The reinforcement cage was then shifted to the wooden box that had the same dimensions as the frame, and the concrete was poured thereafter (Figure 3a). After three days, the formwork was removed, and the frame was moist cured for 28 days. Once sufficient strength was achieved, the frame was shifted to the testing location and positioned vertically for masonry infill construction. The infill wall was constructed in three stages, with approximately one-third of the wall height constructed in each stage (Figure 3b), followed by 28 days of curing. The surface of the masonry wall was made uneven prior to the ECC application to enhance the bond between the substrate and the ECC layer, and a lean cement slurry was applied (Fig. 3c). The ECC layer was applied manually in a manner similar to plastering, in two stages, with each stage covering half the wall length (Figure 3d). Trowelling was performed to ensure uniform thickness throughout the ECC layer.



Figure 3. Construction of masonry infill wall with ECC (a) Casting of the frame (b) brick-laying (c) application of lean cement slurry (d) application of ECC layer by trowelling

2.2 Material characterization

Half-scale burnt clay bricks of dimension 129.2×62.9×40.3 mm and type M1 mortar as specified in IS 1905 (BIS 1987) were used to prepare the masonry walls. The mortar mix of 1:1:6 proportion of cement, lime, and sand was used to prepare the masonry walls. The compressive and tensile strength tests on the brick unit were conducted as per IS 3495 (BIS 1992) and ASTM C1006-13 (2013). The average compressive strengths of the brick were 14.4 MPa (COV=11.5%) and 15.0 MPa (COV=11.1%) for MIF-CS and MIF-EC wall specimens, respectively. The average water absorption was 14.7% (COV=6.2%) by weight. The water-to-binder ratio of the mortar was kept at 0.85 to obtain a workable mortar. The compressive strength of the mortar was obtained by performing the compression test on 50 mm mortar cubes after 28 days of moist curing. The average compressive strengths of the mortar were 8.6 MPa (COV=14.9%) and 5.3 MPa (COV=3.60%) for MIF-CS and MIF-EC wall specimens, respectively. The difference in the compressive strengths of the mortar for both specimens can be primarily attributed to the quality of the hydraulic lime used. The masonry prisms of five stacked bricks were made during construction to investigate the compressive strength of the masonry infill wall. The prism specimens were moist cured for 28 days prior to the testing. The average compressive strengths of the masonry prisms of the MIF-CS and MIF-EC walls were 8.1 MPa (COV=12.0%) and 4.6 MPa (COV=9.6%), respectively. The mechanical properties of the masonry, concrete, and ECC are presented in Table 1. The mixed proportion of the concrete used in the RC member of the MIF-CS specimen was 1:1.58:2.81 with a water-cement ratio of 0.53. The maximum size of the coarse aggregate used in the concrete was 20 mm. As the material used in preparing the MIF-EC was different from that of the MIF-CS specimen, the concrete was designed to get M30 grade of concrete. The concrete was designed using coarse aggregates of 10 mm in size, and the mix proportion of the concrete was 1:2.03:2.42 with a water-to-cement ratio of 0.43. The average compressive strengths of the concrete of the MIF-CS and MIF-EC specimens were 31.3 MPa and 45.3 MPa, respectively (Table 1). The average values of the split tensile strengths of the concrete were 2.5 MPa and 3.0 MPa for MIF-CS and MIF-EC wall specimens, respectively (Table 1). The mix proportion of the cement mortar used for plastering was 1:4 (cement: sand) for both MIF-CS and MIF-EC wall specimens. The average compressive strengths of the cement-sand mortar after 28 days were 15.0 MPa (COV=13.6%) and 11.0 MPa (COV=21%) for MIF-CS and MIF-EC wall specimens, respectively (Table 1). The material properties of masonry prisms, concrete, plaster, and ECC are presented in Table 1. The average yield strengths of 12 mm main reinforcement used in MIF-CS and MIF-EC specimens were 509 MPa and 615 MPa, respectively. The average values of the yield strengths of 6 mm diameter bars used in MIF-CS and MIF-EC specimens were 430 MPa and 589 MPa, respectively.

Table 1. Material properties of the specimens

Specimen	Plaster	Masonry Prism		Concrete		ECC		
	Comp. strength (MPa)	Comp. strength (MPa)	Elastic Mod. (MPa)	Comp. strength (MPa)	Tensile strength (MPa)	Comp. strength (MPa)	Tensile strength (MPa)	Tensile Ductility (%)
MIF-CS	15.0 (13.6)	8.1 (12.0)	2628 (43)	31.3 (7.0)	2.5 (16)	-	-	-
MIF-EC	11.0 (21)	4.6 (11.1)	2489 (19.4)	45.3 (8.3)	3.0 (25)	23.8 (8.2)	2.1 (14.8)	2.1 (21.8)

Values in bracket () presents the COV.

A cost-effective ECC was developed using locally available polyester fiber, which was 10 times cheaper in the local market and approximately 4 times weaker than PVA fibers. The polyester fiber used in the present study was available in the local market under the brand name Recron 3S and was supplied by Reliance Industries Ltd. (Mumbai, India). The other ingredients used in ECC were Portland pozzolana cement (PPC), fly ash (FA), river sand, and polycarboxylate-based high-range water-reducing admixture (HRWRA). The mixed proportion of the

ECC is presented in Table 2. The optimum dosage of HRWRA was 2% to obtain a workable ECC. The optimum dosage of the fiber was decided based on the micromechanical analysis, and it was found that the 3% volume of fiber addition yielded multiple cracking and strain hardening behaviours of ECC. More insights about materials and the process involved in developing the ECC can be found in the previous research of the authors published elsewhere (Kumar and Rai 2022, 2023). The effectiveness of the ECC in strengthening the masonry infill RC frame was verified by testing the specimens under combined in-plane and out-of-plane loads. The mixed proportion of the ECC is presented in Table 2.

Table 2. Mixed proportion of ECC (by weight)

Cement (PPC)	Sand	Fly ash	Water	HRWRA	Polyester fiber (by volume)	Average spread-flow diameter (mm)
1	0.6	1.5	0.65	0.02	3.0 %	148

A uniaxial tensile test was conducted on dog-bone tensile coupons prepared according to the JSCE recommendation for high fiber reinforced cement composites (HPFRCC) (JSCE 2008) to evaluate the tensile performance of ECC (Figure 4a). The uniaxial tensile test was performed using a hydraulic Universal Testing Machine (UTM) with a capacity of 100 kN, under a displacement rate of 0.5 mm/min to simulate quasi-static loading. The tensile stress vs strain of the ECC in Figure 4a shows its strain-hardening behaviour, with an average tensile strength of 2.1 MPa and 2.1% tensile ductility (Table 1). The ECC exhibited multiple cracking and strain hardening behaviour under pure tension (Figure 4a). Additionally, a compression test was performed on cylindrical specimens (100 mm diameter, 200 mm height) in accordance with ASTM C469-02 (Figure 4b). The average compressive strength of the ECC from the cylindrical specimen was 18.35 MPa (COV=13.1%). The average value of the elastic modulus of the ECC obtained from the experiment was 14736 MPa (COV=9.2%). The average compressive strength of the ECC was 23.8 MPa when tested with cubical specimens of dimension 70.6 × 70.6 × 70.6 mm in accordance with IS 4031 (BIS 1988).

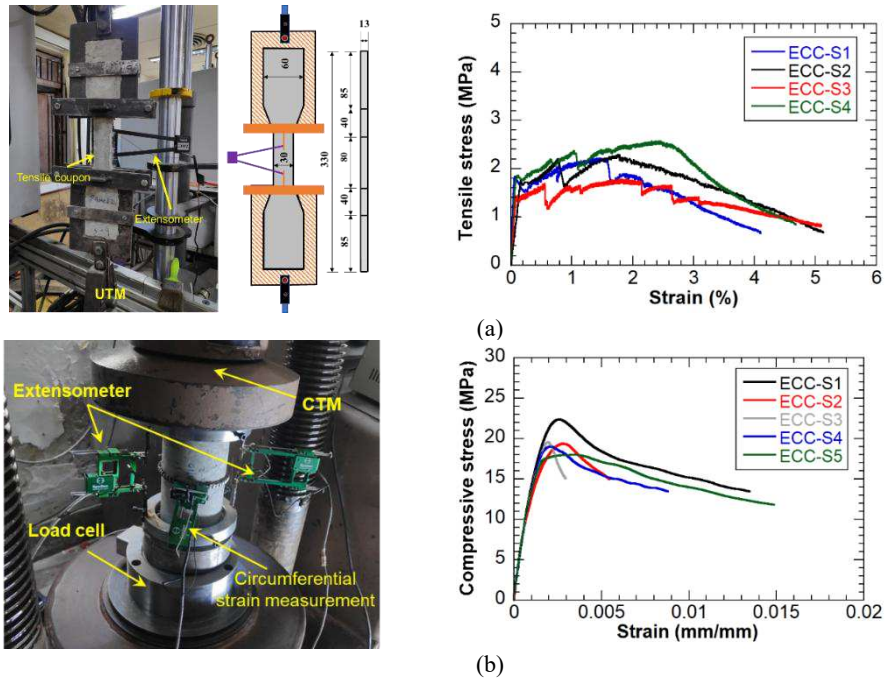


Figure 4. Behavior of ECC under (a) uniaxial tension and (b) compression

2.3 Artificial mass simulation

As explained earlier, the simulated ground motion was applied in the out-of-plane direction to the half-scale masonry infilled RC frame model. A suitable similitude relation is essential for correlating the experimental results of a reduced-scale model with the prototype. For the scaled models, the similitude rules need to be satisfied to

simulate the inertial forces. Artificial mass was added to the model as per similitude laws by attaching the heavy lead blocks to the wall of the specimen, as shown in Figure 5. The requirement of the extra density in the model can be determined from Equation 1 (Tassios 1992). The final adopted similitude laws for the model are shown in Table 3.

$$\Delta m = m_m \left(\frac{1}{S_l} - 1\right) \tag{1}$$

It was found that the additional weight to be added was equal to the mass of the masonry wall. Lead blocks of 60 mm diameter, 28 mm height, and 0.865 kg of average weight were used as the additional mass. Since the average weight of the half-scaled brick was approximately 0.44 kg, one lead block was attached to the wall that served as the artificial mass for the two bricks. The additional weight of the mortar on each side of the infill wall was calculated, and the additional weight requirement was calculated accordingly. A total of 468 lead blocks were required for both MIF-CS and MIF-EC walls to meet the additional weight requirements. These lead blocks were arranged in a regular grid pattern on both faces of the wall in order to avoid any eccentric loading in the out-of-plane direction. These lead blocks were mounted on bolts of 4 mm diameter, which were fixed in the holes drilled in the wall using epoxy glue. Two lead blocks were attached to each bolt and arranged in a regular grid pattern, as shown in Figure 5.

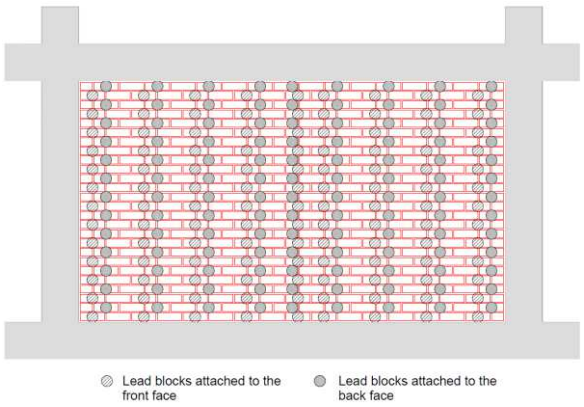


Figure 5. Typical arrangement of the lead blocks on the wall for artificial mass simulation

Table 3. Similitude laws for the masonry arch model used in the study with added mass

Parameter	Scale factor	Replica model value
Length scale ratio, S_l	l_m/l_p	1/2
Modulus ratio, S_E	E_m/E_p	1
Acceleration scale ratio, S_a	a_m/a_p	1
Time scale ratio, S_t	t_m/t_p	1/√2
Frequency scale ratio, S_ω	ω_m/ω_p	√2
Stress ratio, S_σ	S_E	1
Strain ratio, S_ε	$\varepsilon_m/\varepsilon_p$	1

2.4 Test setup and instrumentation

The loading procedure involved the successive applications of in-plane and out-of-plane loading. The test setup was made in such a way that the specimen was not disturbed during the repeated cycle of in-plane and out-of-plane loading. The schematic of the test arrangement is presented in Figure 6. As illustrated in Figure 6a, out-of-plane loading was applied using a servo-hydraulic uniaxial shake table with a platform size of 1.8 m × 1.2 m (Sinha and Rai, 2009). In-plane loading was applied using a 500 kN servo-hydraulic actuator, connected to both ends of the top beam via four high-strength steel rods of 20 mm diameter (Figure 6b). To simulate realistic boundary conditions commonly observed in buildings, where flexible floor or roof diaphragms allow relative displacement between the top and bottom of the wall in the out-of-plane direction, lateral supports were provided on both sides of the specimen. These supports were braced at the top to ensure adequate lateral restraint under both in-plane and out-of-plane loading conditions. The in-plane supports were provided to transfer the overturning loading without affecting the bearing of the shake table. The bearing attached to the top of the support facilitated the smooth in-plane movement of the wall. The gravity load was applied to the infill wall and the columns with the help of the flexible wires. The columns were loaded through a hydraulic jack to a value of 25 kN. The infill

was loaded at four locations with equal spacing to a value of 4.5 kN to get a uniform pre-compression of 0.1 MPa over the infill wall.

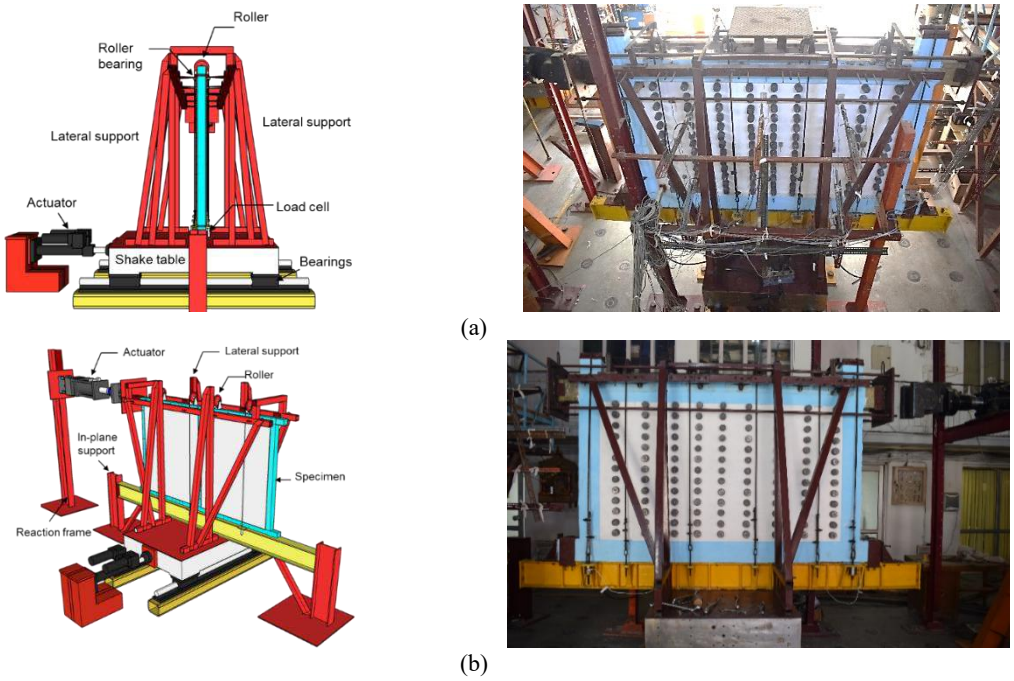


Figure 6. Typical test setup of the specimen for (a) out-of-plane loading and (b) in-plane loading

A typical instrumentation detail of out-of-plane and in-plane loading conditions is presented in Figure 7a and Figure 7b, respectively. 17 accelerometers were used in out-of-plane testing, out of which 16 accelerometers were mounted on the wall. One was fixed on the shaking table, and another was placed directly on the centre of the top beam (Figure 7a). The out-of-plane displacements were measured along the height and length of the wall with the help of 9 linear variable differential transducers (LVDTs) and one string (wire) potentiometer, as shown in Figure 7a. Six load cells were used to measure the variation in the vertical compressive loads on the wall during testing. A total 5 LVDTs were used to measure the in-plane displacement of the wall, as shown in Figure 7b. 4 LVDTs were placed along the height of the wall at various levels on the west end of the wall, whereas one LVDT was placed near the loading position in order to monitor the lateral movement of the actuator on the east side of the wall.

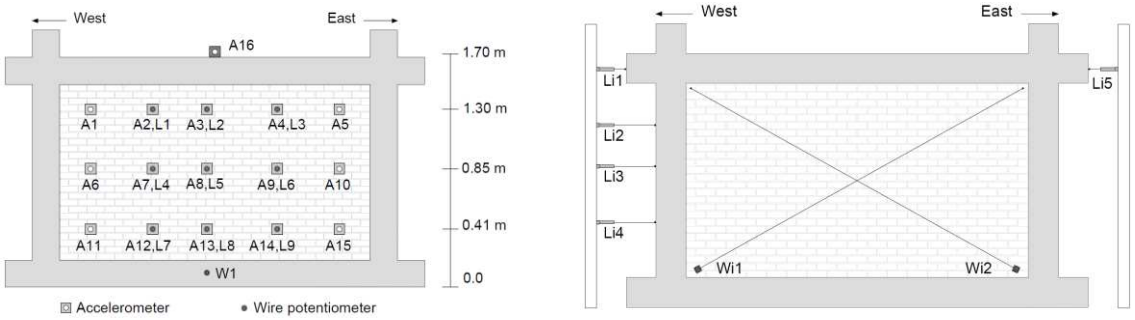


Figure 7. Typical instrumental details for (a) Out-of-plane test (b) In-plane test (A=Accelerometer, W=Wire Potentiometer, L=LVDT, Li=LVDTS for in-plane test)

A total of 4 wire potentiometers were used to record the diagonal deformation of the wall panels. Out of 4 wire potentiometers 2 were along the diagonals to monitor the deformations along the diagonals as shown in Figure 7b. Additionally, a total 6 numbers of load cells were used to monitor the axial loads applied to the wall through

flexible wires (Figure 6a). Sensor data were recorded using a high-performance data acquisition system, with sampling rates of 1000 Hz for dynamic tests and 200 Hz for cyclic tests.

2.5 Loading procedure

During earthquakes, masonry walls are subjected to simultaneous in-plane and out-of-plane loading, which significantly influences their structural response. The specimens behave differently when they are subjected to dynamic loading and monotonic loading. Cracks that open in the specimens during dynamic loading are expected to close automatically when the loading direction changes, potentially resulting in a more stable condition compared to applying a continuously increasing load. Komaraneni et al. (2011) proposed a testing method for brick wall specimens that involved applying out-of-plane and in-plane loads without moving the specimen. Dynamic out-of-plane loads were applied using a shaking table, while in-plane loads were applied slowly with a servo-hydraulic actuator to simulate quasi-static conditions. The pseudo-static in-plane cyclic loading was employed because the dynamic testing will require a larger inertia force for the failure of the specimen, which may exceed the available capacity of the testing facility. The specimens underwent shake table testing with out-of-plane ground motion using the N21E component of the 1952 Taft earthquake, which had a PGA of 0.156g and lasted 54.16s. Only the first 30s, containing the strong motion portion, were used (Figure 8a). The time scale was shortened to meet the similitude criteria, reducing the duration to 21.2s (Figure 8b). The Taft motion was scaled to a PGA of 0.4g to align with the design response spectrum for a design basis earthquake (PGA of 0.36g) per Seismic Zone V of the Indian Seismic Code IS 1893 (BIS 2016) (Figure 8c).

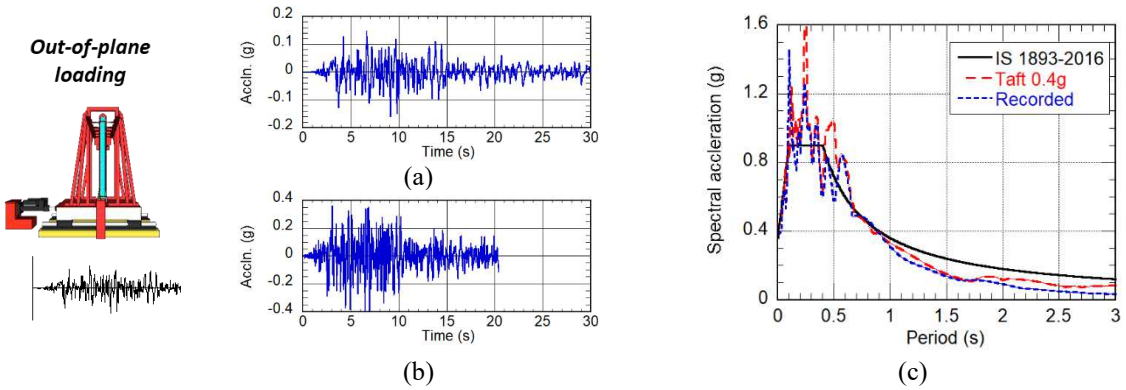


Figure 8. Out-of-plane loading (a) Original Taft N21E ground motion, (b) Scaled Taft motion recorded by shake table, and (c) Comparison of scaled DBE response spectra as per IS 1893 (2016), original Taft motion scaled to 0.4g and recorded Taft motion on shake table

India has four seismic zones (II to V), with Zone V being the most severe. The maximum expected PGAs for each zone are presented in Table 4. The scaled motions are categorized as Level II to Level V, with a lower Level I motion at a PGA of 0.055g also included in the study. Figure 8c compares the design spectra of the Indian seismic code, the response spectra of the scaled Taft motion of 0.4g PGA, and the recorded Taft motion on the shake table. A low-intensity white noise test (0.05g PGA) tracked fundamental frequency changes after loading cycles. Slow cyclic loading was considered in accordance with ACI 374.1-05 (ACI 2005). The specimen was subjected to displacement-controlled loading along the in-plane direction with gradually increased story drift (displacements) of 0.20%. 0.25%, 0.35%, 0.50%, 0.75%, 1.00%, 1.40%, 1.75%, and 2.20% as shown in Figure 9. Each cycle was run three times for each drift ratio. The test commenced with loading the specimen in an out-of-plane direction with Taft ground motion of intensities Level I to Level V, with a white noise test in between. The specimen was then loaded along the In-plane direction in the form of a slow cycle drift to simulate the quasi-static condition. The first In-plane cyclic load continued till the first crack occurred, which was typically 0.5% (Δ_{cr})for the masonry specimens (Singhal and Rai 2014). In the second cycle of out-of-plane loading, the specimen was

subjected to design-level ground motion (Level V Taft), with white noise applied both prior to and following the ground motion. In the second cycle of in-plane loading, the specimen was subjected to 0.75% drift ($0.75\% = 1.5\Delta_{cr}$).

Table 4. PGA values of the scaled Taft ground motion corresponding to the various seismic zones as per IS 1893 (2016)

IS 1893 (BIS 2016)		**Scaled Taft Ground Motion**	
Seismic Zone	PGA (g)	Corresponding matched Taft PGA (g)	Designation during Testing
V	0.36	0.40	Level-V
IV	0.24	0.266	Level-IV
III	0.16	0.177	Level-III
II	0.10	0.111	Level-II
-	-	0.055	Level-I

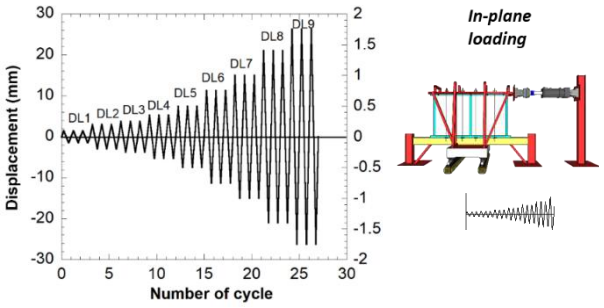


Figure 9. Loading history of the in-plane test

Figure 10 depicts the progressive out-of-plane and in-plane loading until the specimen failed. The specimen was assumed to have failed when significant damage to the column or the wall occurred, leading to a considerable decrease in load capacity. The specimen was also assumed to fail when it underwent large displacement, which resulted in a collapse-like situation. In-plane drift levels were labelled DL (drift level), while out-of-plane loading was denoted by DS (damage state), as shown in Figure 10. The specimen experienced 10 in-plane drift levels (DL1 to DL10) and eight out-of-plane damage states (DS1 to DS6). Damage was recorded after each load cycle, and cracks were marked.

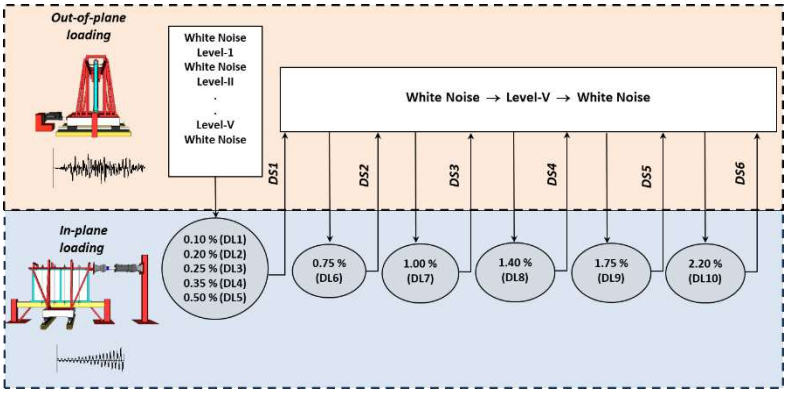


Figure 10. Loading procedure adopted in the test (DL= in-plane drift level and DS= Damage state)

3. RESULTS AND DISCUSSION

The physical observations during the test include the details of cracks developed on the wall and columns, separation of the wall-to-column interface, crushing of concrete, cracking and debonding of the ECC layer, and damage to the column rebar. The details of cracks that occurred on the walls at the end of the test are presented in Figure 11. The detailed cracking sequence of the wall specimen is presented in this section. It was observed that most of the cracks on the wall occurred during the In-plane loading. No new cracks were observed during out-of-plane loading.

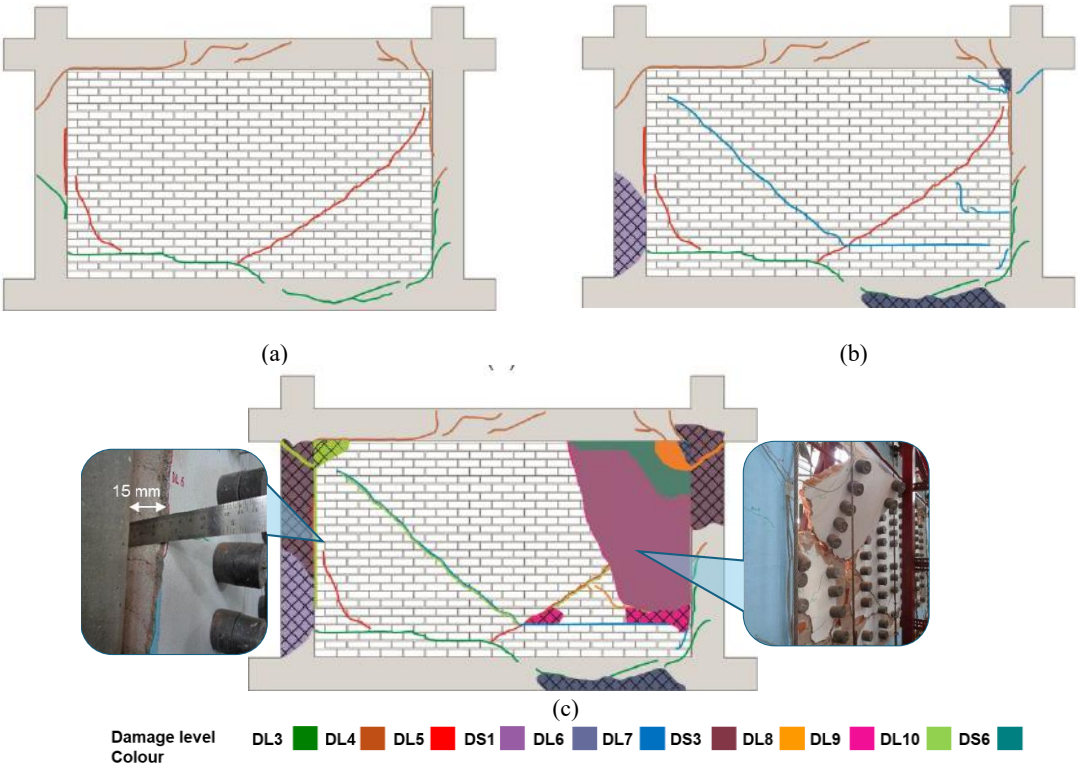


(a) (b)

Figure 11. Failure pattern of the walls at the end of the test of the specimens: (a) MIF-CS and (b) MIF-EC

3.1 Physical observation during the test

The combined in-plane and out-of-plane testing of the MIF-CS specimen was previously conducted by Sagar et al. (2017). The progression of crack development is illustrated in Figure 12. An initial bed joint crack at the wall base and minor plaster cracking on the frame were observed during the 0.25% drift cycle (Figure 12a). At 0.5% drift, diagonal cracking developed in the infill, extending from the top of the east column to the mid-span of the bottom beam, accompanied by minor cracks at the top of the east column. During the 0.75% drift cycle, corner crushing near the top of the east column and separation cracks at the frame–infill interface on the back face were noted. A prominent diagonal crack from the top of the west column to the beam centre, along with additional joint cracking at the base, formed at 1.0% drift (Figure 12b).



(a) (b)

(c)

Figure 12. Sequence of damage of MIF-CS specimen: (a) 0.5% drift (DL5), (b) 1.0% drift (DL7), and (c) end of the test (Sagar 2015)

Subsequent out-of-plane loading caused the detachment of plaster from the frame. At 1.4% drift, a major shear crack developed at the top of the east column, along with extensive toe crushing of the infill panel, significantly reducing the in-plane load capacity. In the positive loading direction, the in-plane force was resisted solely by the frame due to complete debonding between the infill and frame. In contrast, in the negative direction, both the infill and frame contributed to resistance, resulting in asymmetric hysteretic behaviour. Further in-plane loading caused

renewed diagonal cracking and rocking of the infill panel along pre-existing cracks. Severe shaking during subsequent out-of-plane excitation led to the collapse of masonry fragments near the top of the east column (Figure 12c). At 2.2% drift, a shear crack formed at the top of the west column, along with brick crushing at the corner, leading to a significant drop in lateral resistance. By the end of the test, the infill panel had fully separated from both columns, and severe damage was observed in the frame, including rebar buckling. The MIF-EC specimen was first subjected to out-of-plane excitation using Level I to Level V Taft ground motions. The wall exhibited rigid-body movement with no visible damage during this phase. Subsequent in-plane loading was applied incrementally, reaching a maximum drift of 0.5%. The sequence of crack development is shown in Figure 13. Initial cracking was observed at drift level DL4 (0.35%) near the bottom right corner of the east column (Figure 13a). Minor additional cracks appeared near the same region during DL5, corresponding to a peak lateral load of approximately 200 kN.

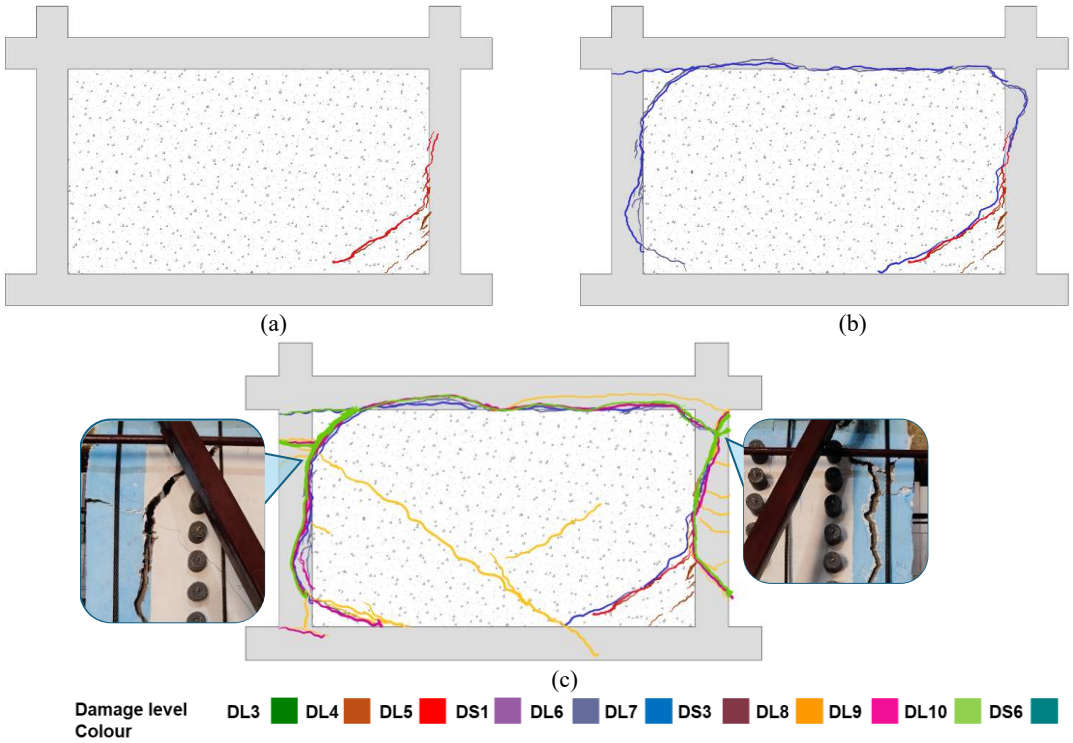


Figure 13. Sequence of damage of MIF-EC specimen: (a) 0.5% drift (DL5), (b) 1.0% drift (DL7), and (c) end of the test

Peripheral cracking was observed during DL6 and widened further in DL7 (Figure 13b), with peak lateral strengths of approximately 238 kN in the positive and 258 kN in the negative direction. These cracks led to partial separation between the infill panel and the surrounding frame. At DL8, a diagonal crack formed from the top of the west column toward the mid-span of the wall (Figure 13c and Figure 14). Despite the development of cracking, the ECC layer effectively controlled the crack width and prevented widespread damage in the infill. However, shear cracks were observed in the RC columns during DL8, indicating a shift in the failure mechanism from infill degradation to frame damage. This led to a significant reduction in lateral load capacity, from a peak of 268 kN to below 100 kN, attributed to shear failure in the columns. In the subsequent in-plane loading cycle, widening of the peripheral cracks resulted in complete detachment of the infill wall from the surrounding frame elements (Figure 13c and Figure 14). As a result, the infill wall ceased to contribute to lateral load resistance. The test was terminated after drift level DL-10 due to a significant reduction in lateral strength. Increased out-of-plane displacements were recorded, attributed to the loss of interaction between the infill and the frame. Despite the detachment, the ECC layer effectively prevented severe damage and collapse of the infill panel. This study primarily aimed to evaluate the effectiveness of ECC in enhancing the seismic performance of masonry infill

walls, particularly at the wall-frame interface, without auxiliary measures such as dowel bars or fiber mesh. Although the ECC layer improved the overall damage tolerance, it was unable to prevent interface cracking due to its moderate tensile strength and the limited bridging capacity of the short fibers. The failure was initiated at the infill-frame interface, highlighting the need for improved bond strategies.



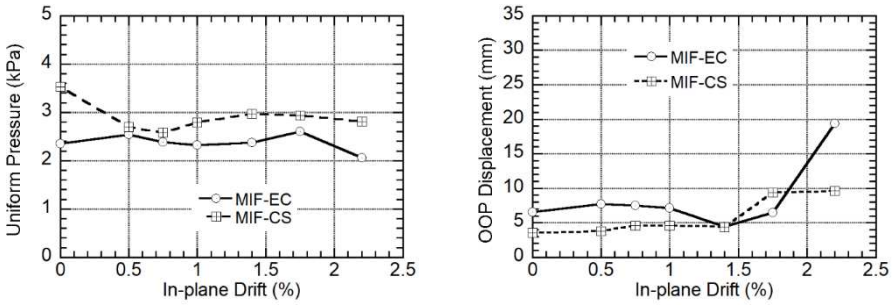
Figure 14. Failure of MIF-EC specimen depicting column failure and separation of infill from frame

3.2 Out-of-plane performance of the wall

The out-of-plane (OOP) accelerations and displacements of the wall were monitored after each level of in-plane (IP) damage. The variation of equivalent uniform pressure, derived from the inertia forces, was evaluated with respect to the IP drift, as shown in Figure 15a. Displacements were measured relative to sensors mounted near the base of the wall specimen (W1 in Figure 7a). The peak inertia force was calculated by multiplying the measured accelerations by the corresponding tributary masses and summing the resulting values across all sensor locations. This total inertia force was then divided by the wall area to obtain the equivalent uniform pressure. The acceleration at each location corresponded to the time when the accelerometer at the centre of the infill panel (A8) recorded its maximum value. MIF-CS specimen experienced a drop in the out-of-plane pressure after 0.5% in-plane drift; however, the out-of-plane pressure remained constant at approximately 3 kPa up to an IP drift of 1.4%. Beyond this point, a reduction in pressure was observed, attributed to a decrease in recorded acceleration resulting from stiffness degradation due to accumulated damage. Diagonal cracks formed in the masonry infill during IP loading led to instability under OOP excitation and ultimately caused collapse of the infill wall at the final stage of testing (Figure 12c). In contrast, the MIF-EC specimen exhibited an average equivalent pressure of approximately 2.4 kPa (Figure 15a). The ECC layer effectively limited crack propagation and prevented fragmentation of the masonry units. Only minor diagonal cracking was observed (Figure 13c). However, the infill panel detached from the surrounding frame after 1.75% IP drift. Unlike the failure observed in the MIF-CS wall, the reduction in OOP pressure in the MIF-EC specimen was primarily due to reduced accelerations resulting from detachment rather than panel degradation.

The average OOP displacements of both specimens are presented in Figure 15b. For MIF-CS, the peak OOP displacements remained nearly constant up to 1.4% drift and increased thereafter, reaching approximately 10 mm at the end of the test due to progressive infill disintegration. However, the excessive cracking of the infill during the in-plane loading caused the collapse of the masonry fragments on the upper right corner. In the MIF-EC specimen, the OOP displacement remained lower up to 1.75% drift, after which it increased, reaching a maximum of approximately 20 mm. This increase was associated with detachment from the frame; however, the ECC layer ensured the structural integrity of the infill panel by preventing brittle failure and fragmentation. The continued increase in out-of-plane deflection for both specimens, despite identical base acceleration input, indicates that the

observed failure was predominantly driven by instability resulting from excessive lateral deformation, rather than by elevated acceleration-induced inertia forces.



(a) (b)

Figure 15 Variation of (a) uniform pressure and (b) OOP displacements of MIF-CS and MIF-EC specimens with In-plane damage

Accelerations were recorded from accelerometers mounted at various heights on the wall panels (Figure 7a), and the values at each level were averaged. OOP displacements were measured using LVDTs and a wire potentiometer, also shown in Figure 7. The relative OOP displacement at each level was calculated by subtracting the peak displacement recorded at the base from the peak displacement at that level. The distribution of average out-of-plane (OOP) accelerations and displacements along the height of the MIF-CS and MIF-EC specimens is presented in Figure 16.

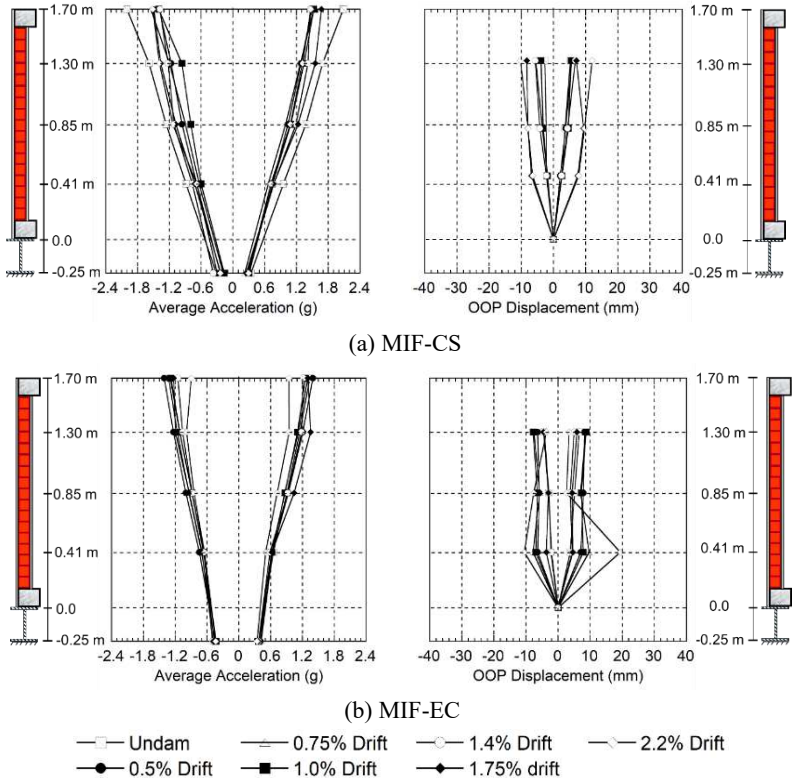
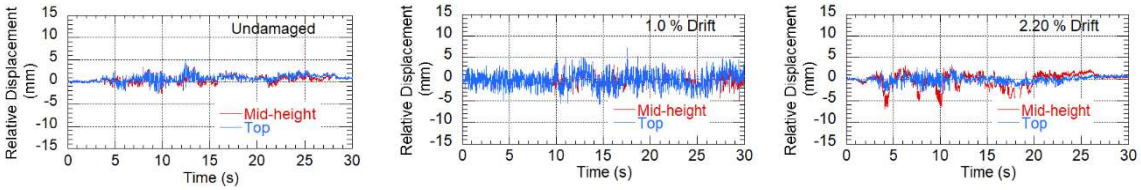


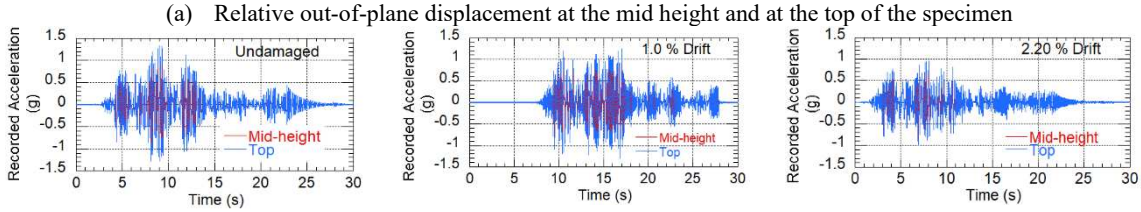
Figure 16 Variation of OOP acceleration and displacements with the height of specimens: (a) MIF-CS (Sagar 2015) and (b) MIF-EC

The acceleration values increased linearly for both specimens, with the maximum amplification of the acceleration at the top. The wall mostly behaved like a rigid wall due to its large stiffness and mass. As shown in Figure 16a, the MIF-CS specimen exhibited higher OOP accelerations in the undamaged state, which gradually decreased with increasing in-plane damage due to progressive cracking of the masonry infill. Correspondingly, OOP displacements increased, reaching a peak of approximately 10 mm by the end of the test. In the MIF-EC specimen, the OOP acceleration profiles remained nearly constant across all damage states, attributed to the limited cracking

of the infill wall due to the confining effect of the ECC layer. The OOP displacements were approximately 10 mm throughout, except during the final damage state, where a nonlinear response and a significant increase in displacement were observed, primarily due to the detachment of the infill panel from the surrounding frame. Despite this detachment, the ECC layer effectively suppressed severe cracking and prevented the disintegration of masonry fragments under OOP loading. The relative OOP displacement and acceleration measured at the mid-height and top levels of the MIF-EC specimen are presented in Figure 17. As shown in Figure 17a, the relative OOP displacements at both levels were nearly identical in the undamaged state, indicating uniform deformation along the wall height. After 1.0% in-plane drift, minor cracking was observed near the infill-frame interface, but no residual displacement was evident, as the displacements at both levels remained comparable. After 2.20% in-plane drift, the infill wall was detached from the surrounding frame, resulting in a higher value of the relative displacements at mid-height and top levels. However, ECC avoided the severe cracking of the masonry infill and thereby protected the masonry fragments from falling. As expected, acceleration increased linearly along the height, with the highest amplification observed at the top of the panel. In the undamaged state, the peak acceleration at the top reached approximately 1.2 g when subjected to the scaled Taft motion (0.4 PGA) (Figure 17b). After 1.0% and 2.20% in-plane drift, a slight reduction in peak acceleration was observed, with the maximum value at the top decreasing to approximately 1.0 g. The reduction is attributed to partial detachment and loss of stiffness at the frame-infill interface.



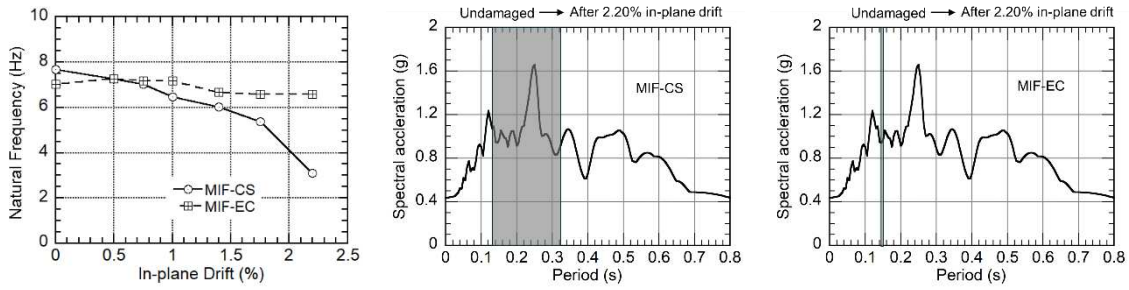
(a) Relative out-of-plane displacement at the mid height and at the top of the specimen



(b) Recorded acceleration at the mid-height and at the top of the specimen

Figure 17 Out-of-plane performance of the MIF-EC specimen

A white noise test was performed before and after the application of out-of-plane ground motion to determine the natural frequency of the wall. The fundamental frequencies of the MIF-CS and MIF-EC specimens were 7.67 Hz and 7.02 Hz, respectively (Figure 18a). The fundamental frequencies of the MIF-EC specimen decreased with in-plane drift primarily due to the accumulated damage that occurred to the specimens during the in-plane loading (Figure 18a). The fundamental frequency of the MIF-EC specimen was almost the same due to the formation of fewer cracks. The fundamental frequency of the MIF-CS specimen dropped to 7.26 Hz after 0.5% in-plane drift due to initial cracking, while the MIF-EC specimen showed negligible change, indicating minimal damage. After 1.4% drift, the MIF-CS frequency reduced by 22% due to diagonal cracking, whereas the MIF-EC specimen showed only an 8% reduction from peripheral cracks. By the end of testing, the fundamental frequencies of the MIF-CS and MIF-EC walls were 3.1 Hz and 6.60 Hz, respectively, representing a 60% reduction for MIF-CS and only 9% for MIF-EC (Figure 18a).



(a) (b) (c)

Figure 18 (a) Variation in the fundamental frequency of CM-CV and CM-SW walls with in-plane drift, and shift in fundamental periods of (b) CM-CV and (c) CM-SW specimens subjected to Taft ground motion

The ECC layer effectively limited stiffness degradation by controlling crack propagation. The shift of the fundamental period of the MIF-CS and MIF-EC specimens with response spectra of Taft ground motion (Level V, PGA=0.4g) is presented in Figure 18b and Figure 18c, respectively. A higher shift in the natural period of the MIF-CS specimen was observed due to excessive damage that occurred to the masonry infill wall (Figure 18b). However, the limited cracking in the MIF-EC masonry infill at various in-plane drift levels resulted in only a minor shift in the natural period (Figure 18c).

3.3 In-plane performance of the walls

The in-plane performance of confined masonry walls was evaluated through peak load capacity, effective stiffness, energy dissipation, displacement ductility, and strength degradation. The results for MIF-CS and MIF-EC walls are summarized in Table 5. The load-displacement envelope curve was idealized as a tri-linear curve to determine effective stiffness and ductility. Experimental ductility is based on yield displacement, typically defined as when reinforcement yields, but can also relate to system behaviour for design. Three limit states were established to idealize the load-displacement envelope curve: cracking limit, maximum resistance, and residual strength (Tomazevic and Klemenc 1997a). The initial stiffness can be determined by $K_e = R_{cr}/\delta_{cr}$ and the yield displacement can be defined as $\delta_y = 0.9\,R_{max}/K_e$. A strength indicator R_w is defined which is taken as 80% of the peak load (R_{max}), which is termed as safe working load, and the corresponding displacement is defined as δ_u. The displacement ductility (μ_Δ) can be obtained by dividing the yield displacement (δ_y) with the post-peak displacement (δ_u). The strength degradation factor C_{sd} is calculated as the ratio of ratio of residual strength (strength at the end of the test), R_r to peak load capacity R_{max}.

Table 5. Summary of the in-plane performance of the specimens

Specimen	Ultimate load, R_{max} (kN)	δ_y^*	$\delta_u^\#$	Effective Stiffness, K_e (kN/mm)	Cumulative energy dissipated (kN m)	Displ. Ductility, μ_Δ	Strength degradation , C_{sd}
MIF-CS	+228.0	+4.0	+25.0	51.3 (+)	54.8	6.2 (+)	0.38 (+)
	-226.4	-3.3	-33.5	61.7 (-)		10.0 (-)	0.59 (-)
MIF-EC	+275.7	+5.9	+23.0	42.3 (+)	40.0	3.9 (+)	0.26 (+)
	-267.8	-5.6	-22.5	43.0 (-)		4.0 (-)	0.30 (-)

δ_y^*= yield displacement
$\delta_u^\#$=post-peak displacement corresponding to R_w i.e., 80% peak load

Figure 19 presents the lateral load–displacement hysteresis curves from in-plane cyclic tests on the MIF-CS and MIF-EC specimens, with positive and negative directions denoting push and pull, respectively. Observed inelastic mechanisms included concrete crushing (C_c), wall rocking (R), column shear cracking (S_c), wall-column separation (S), reinforcement buckling (B), shear sliding (S_s), and reinforcement fracture (F). The MIF-EC wall, strengthened with ECC on one side, exhibited a higher peak load (275 kN) compared to MIF-CS (228 kN). The

in-plane hysteretic responses of both walls were different, as the failure modes of both walls were different. The infill wall of the MIF-CS specimen underwent progressive damage under increasing in-plane drift, leading to a substantial reduction in out-of-plane stiffness. At higher drift levels, the infill lost its load-carrying capacity, and the surrounding RC frame became the primary lateral load-resisting element. A significant reduction in lateral strength was observed due to shear cracking of the columns, as shown in Figure 19a. The MIF-EC specimen demonstrated enhanced lateral strength, primarily due to the presence of the ECC layer, which limited the formation of diagonal cracks and modified the failure mechanism (Figure 19a). However, at larger drift levels, partial detachment of the infill panel from the surrounding frame reduced its effectiveness in resisting in-plane loads, transferring the lateral demand to the frame. A pronounced drop in lateral strength was again observed following column shear cracking (Figure 19b).

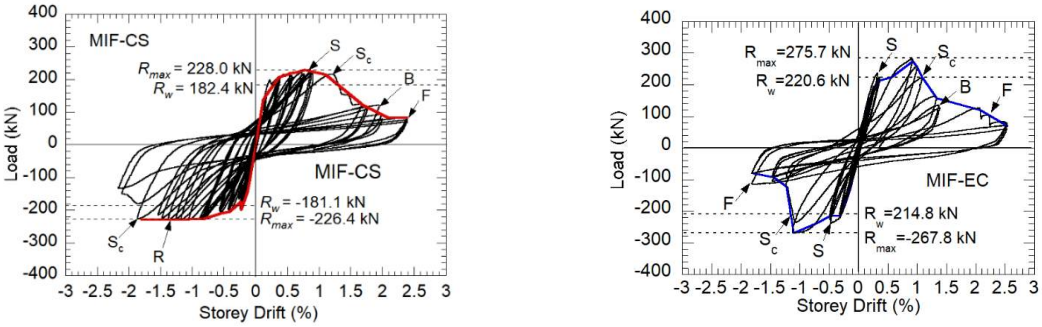


Figure 19 Comparison of hysteretic behaviour of MIF-CS and MIF-EC walls (R= rocking of wall panel, S=Separation of wall to tie column interface, S_c=shear cracking of column, S_s=shear sliding of wall, B=buckling of column reinforcement, F=Fracture of reinforcement)

At advanced drift levels, both specimens exhibited severe column damage, including buckling of longitudinal reinforcement and fracture of lateral ties. The in-plane performance of the MIF-CS and MIF-EC specimens was compared using envelope curves derived from the first-cycle peak displacements at each loading step (Figure 19). The MIF-EC wall showed a 21% increase in peak lateral strength over MIF-CS due to the ECC layer, though the overall envelope response remained similar (Figure 20a). A sudden strength drop in the MIF-EC specimen occurred in the negative direction due to column shear cracking. The lateral response of the bare frame is also plotted, and this was theoretically obtained using SAP 2000 (CSI 2009). The envelope curves of the MIF-CS and MIF-EC approach the theoretical bare frame response after the shear cracking of the column, as shown in Figure 20a. At small displacement levels, the ECC layer maintained a good bond with the masonry substrate, contributing to improved performance. However, at larger displacements, cracking occurred at the frame-infill interface, leading to partial detachment of the infill panel. This detachment was primarily due to insufficient anchorage between the ECC layer and the surrounding frame elements. As a result, the infill's contribution to lateral load resistance diminished, and the frame alone carried the load. The onset of shear cracking in the columns led to the observed sudden reduction in lateral strength. Since the specimens were prepared separately and had different material properties, their lateral strengths were normalized with respect to their bare frame capacities, as shown in Figure 20b. The normalized envelopes of both specimens were similar; however, the lateral capacity of the MIF-EC specimen was greater than that of the MIF-CS specimen. The idealized trilinear plots were obtained from the envelope curves of the MIF-CS and MIF-EC specimens based on the limit states as proposed by Tomazevic and Klemenc 1997a. The comparison of the average tri-linear plots of the MIF-CS and MIF-EC wall specimens is presented in Figure 20c. The key parameters obtained from the idealized tri-linear plots for the MIF-CS and MIF-EC wall specimens are also summarized in Table 5. The peak lateral response of the MIF-EC was approximately 20% greater than that of the MIF-CS specimen due to the use of the ECC layer on the single side

of the wall. The average values of displacement ductility of MIF-CS and MIF-EC specimens were 8.1 and 3.95, respectively. The displacement ductility and strength degradation factor of the MIF-EC specimen were lower because the specimen failed due to the separation of the infill wall from the frame and the shear cracking of the column.

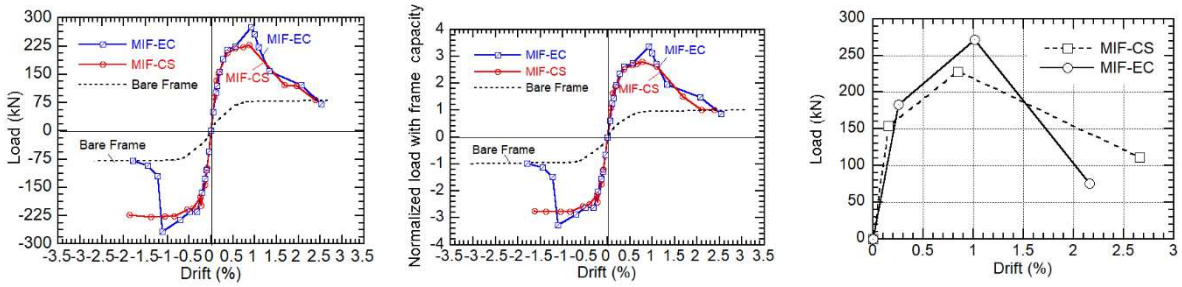


Figure 20 Comparison of in-plane performances of the MIF-CS and MIF-EC walls:(a) failure envelope (b) Normalized lateral load with frame capacity, and (c) idealized tri-linear load-displacement plot motion

The energy dissipated in each loading cycle was estimated from the area enclosed by the hysteresis loops. The cumulative energy dissipation versus in-plane drift for the MIF-CS and MIF-EC specimens is shown in Figure 21a, with corresponding values summarized in Table 5. The total energy dissipated by the MIF-CS and MIF-EC specimens was 54.8 kNm and 40.0 kNm, respectively. The higher energy dissipation in the MIF-CS specimen is attributed to the formation of numerous fine cracks and shear sliding in the masonry, which enhanced energy absorption. In contrast, the MIF-EC specimen exhibited fewer cracks due to the ECC layer, and failure was primarily governed by infill-frame separation, resulting in lower overall energy dissipation. The cumulative energies of both specimens increased with the in-plane damage. The rise in the cumulative energy dissipation curves was similar for both specimens. However, the MIF-CS specimen showed a steeper rise due to the occurrence of more cracks on the infill wall panel. However, the presence of larger cracks on the infill panel MIF-CS wall specimen decreased the out-of-plane strength and caused the collapse-like failure of the infill wall during the out-of-plane loading. The damping characteristics of the MIF-CS and MIF-EC walls were quantified using equivalent viscous damping (ζ_{eq}), calculated from the hysteresis loops as illustrated in Figure 21b. ζ_{eq} is defined as the ratio of energy dissipated in a hysteresis cycle (E_D) to the maximum strain energy of an equivalent elastic system (E_s). The variation of ζ_{eq} with in-plane drift. Equivalent damping increased with progressive damage in both specimens due to cracking of the infill, column shear cracking, reinforcement yielding, and crushing of wall panels (Figure 21b). At the end of testing, ζ_{eq} reached 20.8% for MIF-CS and 20.1% for MIF-EC. The slightly higher damping in MIF-CS is attributed to the more extensive cracking in the masonry infill. Theoretical estimates of ζ_{eq} were also obtained using the method proposed by Priestley et al. (2007), yielding values of 17.4% for MIF-CS and 15.6% for MIF-EC. These estimates closely matched experimental values, with an error range of 17-23%, suggesting that the method provides reasonable predictions for damping in ECC-strengthened and unstrengthened masonry walls and can be used in seismic design.

The cyclic stiffness (K_i) of the MIF-CS and MIF-EC specimens was evaluated at various in-plane drift levels, as shown in Figure 21c. Stiffness values were normalized with respect to the initial stiffness to quantify degradation due to cumulative damage. The variation in stiffness with drift is presented in Figure 21c. Both specimens exhibited similar stiffness degradation trends. At 0.5% drift, the cyclic stiffness of MIF-CS and MIF-EC reduced to 37.9% and 39.2% of their initial values, respectively. Beyond 1.40% drift, a substantial loss in stiffness was observed, with values dropping to 10.9% for MIF-CS and 10.2% for MIF-EC, corresponding to severe damage in the masonry infill and partial detachment in the ECC-strengthened wall. At the end of testing, the cyclic stiffness

values further reduced to 3.5% for MIF-CS and 3.3% for MIF-EC, indicating that the lateral load resistance was predominantly provided by the frame at higher drift levels. Figure 21d shows the post-peak in-plane strength degradation of MIF-CS and MIF-EC specimens, calculated as the ratio of lateral strength at each cycle to the peak strength. Both specimens showed a progressive decline due to accumulated damage. By the end, MIF-CS and MIF-EC specimens retained 48% and 28% of their peak strengths, respectively.

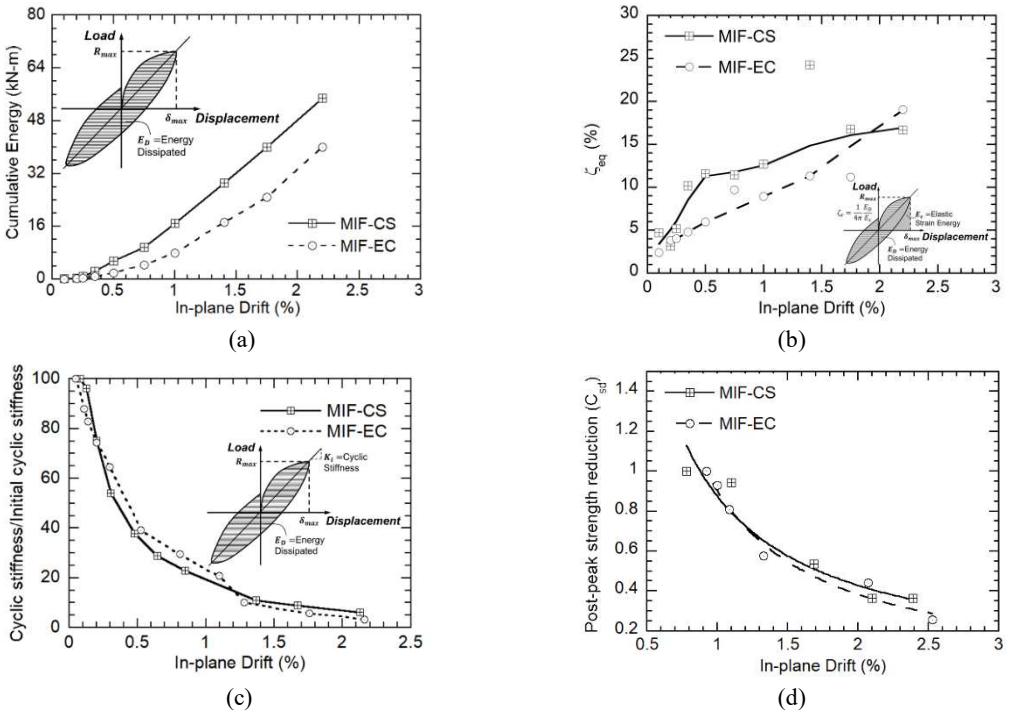


Figure 21 In-plane hysteretic response (a) cumulative energy dissipation (b) equivalent viscous damping (c) cyclic stiffness degradation, and (d) strength degradation

3.3 Axial compression in the wall

As previously described, a vertical compressive stress of 0.1 MPa was applied to the wall using flexible wires to simulate gravity loading. This load was introduced at four equidistant points along the top of the wall, and its variation during testing was continuously monitored using load cells. The axial loads recorded by the load cells were averaged and normalized with respect to their initial values, and the variation in axial load levels during the in-plane and out-of-plane tests was plotted (Figure 22). Variations in the axial load are primarily attributed to wall elongation during the rocking motion, which was restrained by the flexible wires. The average normalized axial load from the four load cells was plotted against the mid-height out-of-plane displacement relative to the shake table, as shown in Figure 22a. The results indicate that the axial load variation remained within approximately ±1% during the out-of-plane shake table test, which was conducted following in-plane loading up to a drift level of 0.5%. The variation in axial load levels after each in-plane drift, as shown in Figure 22b, indicates that the maximum change occurred at the highest drift level (2.20%) when the infill was completely detached from the surrounding frame. During the in-plane cyclic loading, the axial load on the wall increased due to the additional tension induced in the flexible wires by the overturning moment. At lower drift levels, the axial load in the flexible wires remained nearly constant, with a variation of only about 3% observed at DL-2 (0.2% in-plane drift) (Figure 22c). However, at a drift level of 1%, the axial load increased by approximately 30% relative to the initial value, primarily due to the additional tensile forces induced in the wires by the overturning moment (Figure 22d).

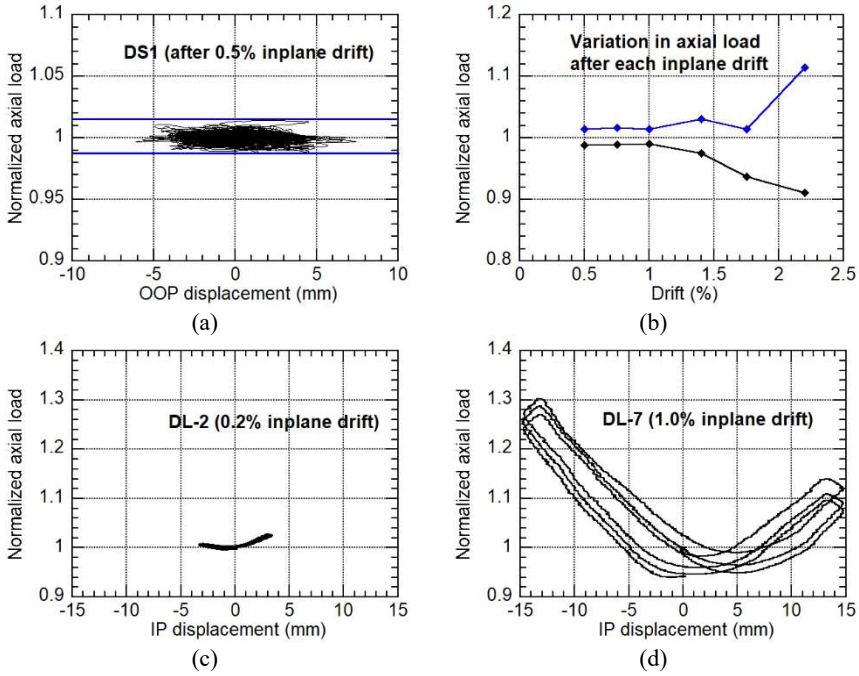


Figure 22 Variation of the axial load levels during the test: (a) normalized axial load vs relative out-of-plane mid-height displacement, (b) normalized axial load vs in-plane drift during out-of-plane loading, (c)and (d) normalized axial load vs in-plane displacement at the top for two drift levels, 0.2 and 1%, respectively

4. ANALYTICAL INVESTIGATION

4.1 In-plane Strength of the wall

The shear failure of masonry structures is a typical type of failure during the events of earthquakes due to the geometry of the structural wall and typical material behaviour (Tomaževič 1999). The present study investigates the performance of a masonry infill RC frame structure comprising brick masonry, plaster and an ECC layer under combined in-plane and out-of-plane loading. The in-plane shear strength was estimated by summing the contributions of the frame, masonry, and ECC layer (Figure 23). As observed experimentally, failure initiated with shear cracking in the columns, followed by diagonal cracking in the wall panels. Peak lateral resistance occurred after these cracks, and interaction effects were neglected. Thus, the total lateral strength was taken as the algebraic sum of the individual components (Equation 2).

$$H = H_f + H_m + H_P + H_{ECC} \tag{2}$$

The lateral strength of the column is primarily due to the dowel action of the vertical rebars, shear resistance provided by the link bars, and interlocking of aggregate (Figure 23). The shear resistance of the column was considered as the sum of the shear strength from vertical rebar dowel action, concrete, and shear reinforcement, following IS 456 (BIS 2000) recommendations, as expressed in Equation 3.

$$T_{ss} = \tau_c \times b \times d + \left(f_y \times A_{sv} \times d/S_v\right) \tag{3}$$

where, τ_c is the shear stress of the concrete, which depends on the grade of the concrete and the amount of main reinforcement, b and d are the width and the depth of the column. f_y, A_{sv} and S_v are the yield strength, cross-sectional area, and spacing of link bars provided in the column. As there were three tie columns in a plane, the lateral resistance provided by the frame was three times the shear strength of the single column ($H_f = 2T_{ss}$).

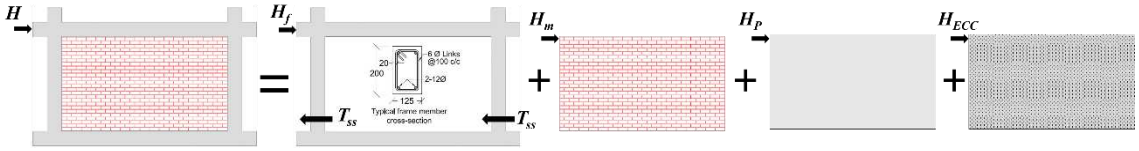


Figure 23 Estimation of lateral strength of the wall

Masonry walls subjected to lateral loads can exhibit various shear failure modes, including shear sliding along mortar joints under low compressive stress, stair-step cracking through bed and head joints in the case of weak mortar and strong brick units, and diagonal tension failure passing through the masonry units in the case of high pre-compression. Experimental observations revealed two primary failure modes in the masonry wall: shear sliding along the bed joints and diagonal cracking, accompanied by fracturing of the brick units. The shear strength of the masonry wall panels was estimated to be based on two major failure modes, shear sliding and diagonal tensile cracking (Figure 24a). The shear strength of the masonry wall from the shear sliding failure mode can be determined using the Mohr-Coulomb failure criterion as per Equation 4.

$$\tau = \tau_m + \mu q \tag{4}$$

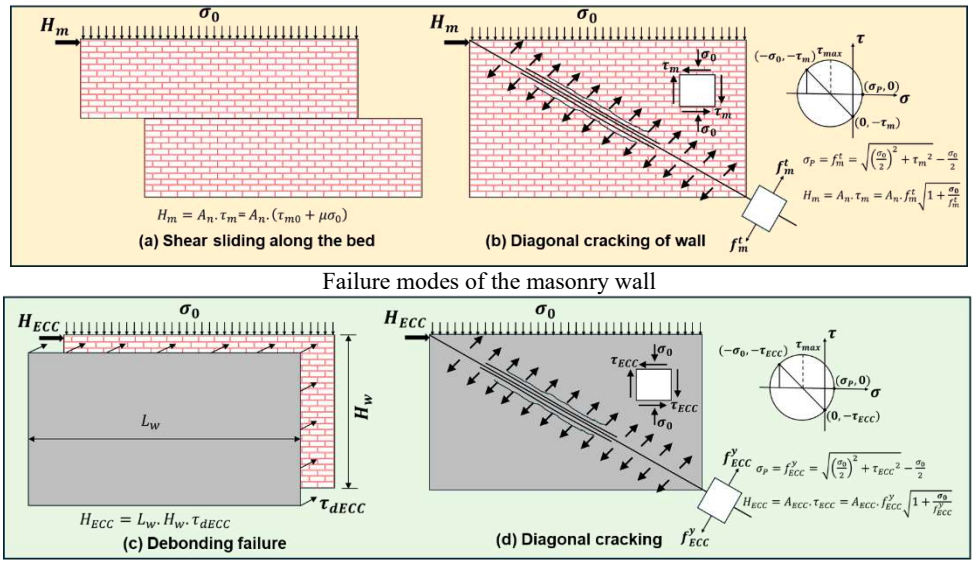
where τ_m is the shear strength obtained from the test, μ is the coefficient of friction, and q is the applied vertical pressure. Shear strength can be determined experimentally or taken from design codes such as Eurocode 6 (CEN 2005) and MSJC (2011). The second most prominent mode of failure of the masonry wall panel is diagonal cracking. When the wall is subjected to both vertical and lateral loads, shear failure is initiated by the formation of diagonal cracks due to principal tensile stresses (Figure 24b). The lateral shear resistance of the masonry wall, assuming it to be a homogeneous and isotropic structural element, can be represented by Equation 5 (Tomaževič 1999).

$$R_w = A_w \left({f_m^{t'}}/{\beta_s} \right) \sqrt{{q}/{f_m^{t'}} + 1} \text{ with } \beta_s = min\left(\frac{H_w}{L_w}, 1.5\right) \geq 1.0 \tag{5}$$

$$R_w = f_m^{t'} A_w \beta \sqrt{1 + {q}/{f_m^{t'}}} \text{ with } \beta = \begin{cases} 0.67 & for \quad L/h_{eff} \leq 0.67 \\ L/h_{eff} & when \; 0.67 \leq L/h_{eff} \leq 1 \\ 1 & when \quad L/h_{eff} \geq 1 \end{cases} \tag{6}$$

where, $f_m^{t'}$ is the tensile strength of the masonry and β_s is the shear stress distribution factor of the wall that depends on the geometry of the wall. A similar formula has been suggested in ASCE-41 (ASCE 2007) for the determination of the lower bound in-plane diagonal tension strength of the masonry wall as given in Equation 6. The minimum shear strength obtained from the shear sliding failure and diagonal crushing criteria was taken as the shear strength of the masonry wall panels (H_m). The predominant failure mode of the masonry wall panel was diagonal crushing. Consequently, the in-plane shear strength due to diagonal crushing failure was deemed the in-plane shear strength of the masonry wall panel. From the experimental investigations, it was found that there could be two major failure modes of ECC, namely debonding failure and shear failure of the ECC layer. The shear strength contribution of the ECC layer can be obtained based on these two failure modes as presented in Figure 24c. As the strengthened wall is subjected to the lateral force, the ECC layer holds the masonry wall from cracking, thus enhancing the lateral strength. The lateral strength contribution of the ECC layer from the debonding failure mode can be given by the bond strength (τ_{dECC}) of the ECC multiplied by the normal surface area of the masonry substrate (Figure 24c). The second most observed mode of failure of the infill wall panel was diagonal cracking. When the wall is subjected to both vertical and lateral loads, shear failure is initiated by the formation of diagonal

cracks due to principal tensile stresses. Figure 24d presents the present state of stress of the ECC layer when the wall is subjected to vertical stress and a shear stress caused by the lateral forces.



Failure modes of the masonry wall

Failure modes of the ECC/Plaster layers

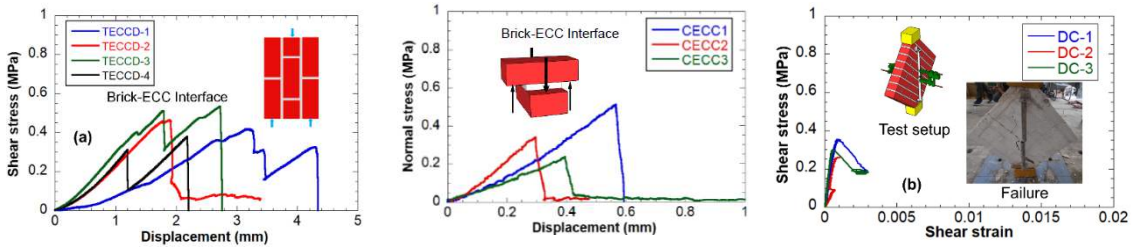
Figure 24. Failure modes of the infill panel considered in evaluating the in-plane strength of the wall

The diagonal cracking of the ECC was caused due to the major principal stress, σ_P, which was obtained from the Mohr's circle as shown in Figure 24d. The in-plane shear contribution of the ECC layer (H_{ECC})can be taken as the minimum of the bond strength and the shear strength from the diagonal cracking of the ECC layer, as given in Equation 7.

$$H_{ECC} = min\begin{cases} L_w.H_w.\tau_{dECC} \\ A_{ECC}.f_{ECC}^{y}\sqrt{1+\dfrac{\sigma_0}{f_{ECC}^{y}}} \end{cases} \quad (7)$$

A similar approach can also be adopted to determine the contribution of the plaster layer to the lateral strength of the wall. However, the interface properties of brick and ECC were obtained experimentally, which can be further used in the above equation to obtain the lateral strength of the wall. Sub-assemblage tests were conducted to obtain the normal and shear characteristics of the interface between the brick and the ECC using the couplet and shear triplet tests. The brick couplet test was performed as per ASTM C952-12 (2012), and the shear triplet test was performed in accordance with BS EN 1052-3:2002. A detailed discussion can also be found in the previously published work by the authors (Kumar and Rai 2024). The shear triplet tests were performed with six brick arrangements, as shown in Figure 25 (a). In the present study, the shear tests were conducted for zero confining pressure, and the peak shear stress corresponding to zero confining pressure was used for numerical modelling. As the regression analysis wasn't conducted, the angle of internal friction could not be obtained. Consequently, the frictional coefficient value of 0.93 was obtained from Singhal and Rai (2014), where tests were conducted on identical bricks and mortar composition. The test setup for couplet tests is shown in Figure 25 (b). It was found that the shear strength of the brick-mortar interface was around 0.3 MPa, and normal bond strength was around 0.2 MPa. For the brick-ECC interface, both shear and normal interface strengths were found to be higher than the brick-mortar interface. The normal interface strength of the brick-ECC interface was found to be around 0.3 MPa, and the shear strength was found to be 0.5 MPa. The diagonal compression was also performed in accordance with ASTM E519 (2010) to investigate the in-plane shear of the masonry (Figure 25). The diagonal tension (shear) capacity of the masonry was found to be 0.31 MPa after the experimental investigation. The experimentally obtained values of the bond stress between the masonry-mortar interface, masonry-ECC interface, friction

coefficient, and the in-plane shear stress of the masonry can be employed in Equations 4-7 to obtain the in-plane strength of the wall.



(a) (b) (c)

Figure 25. (a) Bond test of the brick-ECC (b) diagonal compression test of the masonry

The lateral resistance provided by the frame with 12 mm vertical bars and 6 mm shear links was 155.6 kN. The major lateral strength of the wall is contributed to by the frame due to the stronger frame elements. The lateral strengths of the masonry infill and the 6 mm layer of plaster were 62.8 kN and 10 kN, respectively. It was observed from the experiment that the ECC failed by diagonal shear cracking, and no debonding of the ECC layer was observed. It was also evident from the analytical evaluation that the strength corresponding to the diagonal shear strength governed the shear strength of the ECC. The lateral strength of the 6 mm ECC layer was calculated as 37.6 kN. The lateral strengths of the confined masonry walls obtained from various methods are presented in Table 6 and are compared with the experimental results. It was also observed that the lateral strength obtained from the proposed analytical method closely matched experimental results, as the percentage error varied between 2% and 9%.

Table 6 Comparison of the analytically predicted in-plane strength with experimental results

Specimen	**Analytical Method**					**Experiment**	$H_{Anl.}/H_{Exp.}$
	H_f (kN)	H_m (kN)	H_P (kN)	H_{ECC} (kN)	$H_{Anl.}$ (kN)	$H_{Exp.}$ (kN)	
MIF-CS	114.8	68.7	20.1×2	-	223.7	227.21	0.98
MIF-EC	133.6	68.7	15.8	29.6	247.7	271.7	0.91

4.2 Out-of-plane strength of the wall

Masonry buildings are typically designed for in-plane loads, resulting in poor out-of-plane performance of unreinforced masonry (URM) walls, especially when pre-existing in-plane cracks are present. Accurate assessment of out-of-plane capacity is crucial for seismic safety. This capacity is influenced by boundary conditions, wall slenderness (H_w/t_w), and frame stiffness. Traditional elastic plate theory often underestimates strength due to flexural failure assumptions, while arching action can enhance capacity through compression. Dawe and Seah (1989) proposed an empirical model accounting for arching action and varying boundary stiffness. The uniform pressure q (kPa) of an individual frame can be determined using Equation 8 and Equation 9.

$$q_{DS} = 4.5(f'_m)^{0.75}t^2\left(\frac{\alpha}{l^{2.5}} + \frac{\beta}{h^{2.5}}\right) \tag{8}$$

where,

$$\alpha = \frac{1}{h}(E_c I_c h^2 + G_c J_c th)^{0.25} < 50$$
$$\beta = \frac{1}{l}(E_b I_b l^2 + G_b J_b tl)^{0.25} < 50 \tag{9}$$

The parameters, α and β represent the relative stiffness of the confining columns and beams, respectively. This method was originally developed for concrete masonry with a steel frame and was further modified by Flanagan and Bennett (1999) for clay masonry with a steel frame. The numerical constant in Equation 9 was replaced by 4.1, and the torsional rigidities ($G_c J_c th$ and $G_b J_b tl$) of the frame were eliminated while obtaining the parameters

α and β. The reduction factor to account for prior in-plane damage in out-of-plane capacity was first considered by Abrams et al. (1996). Two reduction factors, R_1 and R_2, were introduced to incorporate the effect of prior damage and the flexibility of the surrounding frames. The maximum uniform pressure can be given by Equation 10.

$$q_{Al} = \frac{2f'_m}{\left(\frac{h_w}{t_w}\right)} R_1 R_2 \, \lambda \tag{10}$$

where,

$$R_1 = \left[1.08 - 0.015\left(\frac{h}{l}\right) - 0.00049\left(\frac{h}{l}\right)^2 + 0.000013\left(\frac{h}{l}\right)^3\right]^{\frac{\Delta}{2\Delta_{cr}}}$$
$$R_2 = 0.357 + 2.49 \times 10^{-14} EI \leq 1 \tag{11}$$

The reduction factor R_1 is introduced as a function of the slenderness ratio (h_w/t_w) to account for the prior in-plane damage, as shown in Equation 11, which may be taken as 1 in the undamaged state. Δ_{cr} is the in-plane drift at which the first crack is visible on the wall. As the first cracking of the confined masonry occurred at 0.5% in-plane drift, the value of Δ_{cr} was taken as 0.5. To account for the flexibility of the surrounding frame, a reduction factor is introduced. This factor is determined by the flexural stiffness (EI) of the smallest member of the confining frame at the panel edge where there is no continuity. Flanagan and Bennet (1999) showed that for the values of h_w/t_w between 10 and 30, the non-dimensional parameter λ can be presented by Equation 12.

$$\lambda = 0.154 \, exp\left(-0.985 \frac{h_w}{t_w}\right) \tag{12}$$

The method was later adopted by FEMA 306 (1998) with slight modifications in the values of the reduction factor R_1, based on damage conditions such as moderate and severe. The numerical coefficient 2 in Equation 10 was later replaced by 0.7 in FEMA 356 (2000) for the existing buildings. The changes were made because the FEMA 356 equation provides a lower-bound strength, accounts for strength reduction due to prior in-plane damage, and assumes a frame stiffness of $1.032 \times 10^{13} \, Nmm^2$, resulting in an R_2 value of 0.61.The uniform out-of-plane pressure ($q_{Exp.}$) obtained from the experiment was compared with the calculated uniform pressure ($q_{Cal.}$) using various analytical methods for the undamaged state (Table 7).

Table 7 Comparison of the out-of-plane capacity of the confined masonry walls obtained using various analytical methods and experiments

Specimen	**MIF-CS**		**MIF-EC**	
Experimental Result	$\boldsymbol{q_{Exp.} = 3.53}$ *kPa*		$\boldsymbol{q_{Exp.} = 2.44}$ *kPa*	
Analytical Method	$q_{Cal.}$ *(kPa)*	$q_{Exp.}/q_{Cal.}$	$q_{Cal.}$ *(kPa)*	$q_{Exp.}/q_{Cal.}$
Dawe & Seah (1989)	5.8	0.61	6.12	0.40
Flanagan and Bennett (1999)	6.0	0.59	6.4	0.38
Abrams et al. (1994)	5.09	0.69	5.9	0.41
FEMA 306 (FEMA 1998)	4.97	0.71	5.4	0.45
FEMA 356 (FEMA 2000)	3.03	1.16	3.33	0.73

The out-of-plane strength of the masonry wall, estimated using the methods proposed by Dawe & Seah (1989) and Flanagan & Bennett (1999), overpredicted the experimental strength by approximately 39% to 60%. The out-of-plane strength of the masonry infill wall calculated using FEMA 356 (2000) gave the best results, as the percentage error was between 16% and 27%. The variation of the out-of-plane strength of the confined masonry walls with prior in-plane damage calculated using methods proposed by Abrams et al. (1996) and FEMA 306 (1998) is compared with the experimental result (Figure 26). The out-of-plane strengths of the MIF-CS wall were calculated at 0%, 0.5%, 1.0%, 1.75%, and 2.20% prior to in-plane drifts. It was observed that the first cracking of the MIF-CS and MIF-EC walls was observed at 0.5% in-plane drift, and the damage at this level could be

considered as moderate, as there were few cracks visible on the wall. There was severe cracking to the wall specimens after 1.40% in-plane drift; hence, the damage state could be considered severe. The analytically estimated out-of-plane pressure in the undamaged state was overpredicted. The experimental out-of-plane loading was insufficient to fully mobilize the wall's out-of-plane capacity, while the analytical model assumed full mobilization, leading to overprediction. At higher drift levels, where the specimens had sustained significant damage, the experimental results showed good agreement with the analytical predictions using the Abrams et al. (1994) model (Figure 26a and Figure 26b).

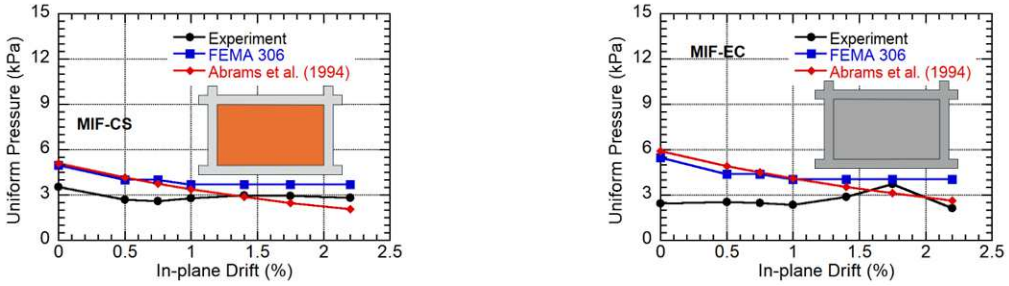


Figure 26. Comparison of OOP pressure obtained from experiment and analytical methods for specimens: (a) MIF-CS (b) MIF-EC

5. CONCLUSIONS

This study proposes a practical strengthening technique for masonry infill RC frame (MIF) structures using Engineered Cementitious Composites (ECC) applied by trowelling. This approach allows for the ECC layer to be applied to the wall surface in a manner similar to traditional plastering techniques. However, a little extra effort is required in trowelling as the wet ECC mix contains a high volume of fibre that makes the mix cohesive. A comprehensive experimental program was conducted to assess the combined in-plane and out-of-plane performance of ECC-strengthened (MIF-EC) and unstrengthened (MIF-CS) masonry infill RC walls. A half-scale MIF wall was strengthened with a 6 mm-thick ECC layer applied to one side and tested under combined loading to evaluate the effectiveness of the proposed technique.

The experimental investigation demonstrated that in-plane damage significantly affects the out-of-plane (OOP) performance of masonry infill RC walls. For the unstrengthened MIF-CS specimen, progressive in-plane cracking led to instability under OOP loading, resulting in collapse at higher drift levels. In contrast, the ECC-strengthened MIF-EC specimen exhibited improved crack control and maintained infill integrity, although detachment from the frame occurred at large drifts. The ECC layer effectively delayed degradation and prevented brittle failure, but anchorage at the frame–infill interface remains critical. The MIF-EC specimen exhibited approximately 20% higher in-plane strength than MIF-CS. While shear cracking in the frame columns governed strength degradation in both cases, severe cracking occurred in the MIF-CS infill, whereas the ECC layer in MIF-EC effectively limited infill damage. However, detachment of the infill from the surrounding frame was observed in the MIF-EC specimen, likely due to limited fiber bridging near the frame–infill interface. The findings indicate that excessive out-of-plane displacements, rather than high inertial forces, were the primary cause of instability. Trowel-applied ECC strengthening effectively enhanced seismic performance by controlling damage and preserving infill integrity under combined in-plane and out-of-plane loading.

A simplified analytical approach was developed to estimate the in-plane strength of masonry infill RC frame structures, aiding in the design of wall panels and confining elements. The method considered shear sliding and diagonal cracking as the primary failure modes based on experimental observations. ECC contribution was

evaluated considering the lower bound of strength from debonding and tensile cracking. Despite neglecting interaction with peripheral elements, the predicted lateral strength closely matched experimental results, with an error margin of 2-9%. The out-of-plane capacity of the specimens was assessed using existing analytical models. Predictions from Dawe & Seah (1989) and Flanagan & Bennett (1999) overestimated the out-of-plane strength in the undamaged state compared to experimental results. In contrast, the analytical predictions based on FEMA 356 (2000) showed reasonable agreement with the experimental results, with an error margin ranging from 16% to 27%.

ACKNOWLEDGMENTS

The authors sincerely acknowledge the financial assistance provided by the Ministry of Education, Government of India, New Delhi. The authors would also like to thank M/S Kuraray Co. Ltd. (Japan), M/S Reliance Industries (Mumbai, India), and M/S Fosroc Constructive Solutions (India) for providing the material for the research. The authors sincerely acknowledge the assistance provided by the staff of the structural engineering laboratory at the Indian Institute of Technology Kanpur.

REFERENCE

1. Abrams, DP, Angel, R, and Uzarski, J. Out-of-plane strength of unreinforced masonry infill panels. *Earthquake Spectra*, 1996; 12(4): 825-844.
2. American Concrete Institute (ACI). Acceptance criteria for moment frames based on structural testing and commentary. ACI 374.1-05, ACI Committee 374, Farmington Hills, MI, 2005.
3. American Society of Civil Engineers (ASCE). American Society of Civil Engineering. Seismic rehabilitation of existing buildings. American Society of Civil Engineers, 2007.
4. ASTM Standard C469/C469M-14. Standard Test Method for Static Modulus of Elasticity and Poisson's Ratio of Concrete in Compression; ASTM International: West Conshohoken, PA, USA, 2014.
5. ASTM C952, Standard test method for bond strength of mortar to masonry units, 2012.
6. ASTM. Standard test method for splitting tensile strength of masonry units. ASTM C1006-13. West Conshohocken, PA: ASTM, 2013a.
7. ASTM E519/ E519M. Standard test methods for diagonal tension (shear) in masonry assemblages, American Society for Testing and Materials (ASTM), West Conshohocken, PA, 2010.
8. Avasthi, R, Kumar, S, Rai, DC. Limit Analysis and Seismic Performance of Mortar-Bonded and ECC Layered Masonry Arches. *Earthquake Spectra*, 2025; 54 (5): 1454-1474.
9. BS EN 1052-3, Methods of test for masonry - Part 3: Determination of initial shear strength, BS EN 1052-3, 2002.
10. Bureau of Indian standards (BIS), Indian standard code of practice for structural use of unreinforced masonry, IS 1905, New Delhi, India, 1987.
11. Bureau of Indian standards (BIS), Methods of tests of burnt clay building bricks., IS 3495, New Delhi, India, 1992.
12. Carozzi FG, Milani G, Poggi C. Mechanical properties and numerical modeling of Fabric Reinforced Cementitious Matrix (FRCM) systems for strengthening of masonry structures. *Composite structures*. 2014; 107:711-25.
13. BIS (Bureau of Indian Standards). Method of physical tests for hydraulic cement-Part 7: Determination of compressive strength of masonry cement. IS 4031. New Delhi, India: BIS, 1988.
14. BIS (Bureau of Indian Standards). Indian standard criteria for earthquake resistant design of structure, Part 1: General provisions and buildings, IS 1893, New Delhi, India, 2016.
15. BIS (Bureau of Indian Standards). Indian Standard Plain and Reinforced Concrete-Code of Practice. IS 456, Fourth revision, New Delhi, India, 2000.
16. CSI (Computers and Structures Inc). Integrated software for structural analysis and design, SAP 2000. Walnut Creek, CA: CSI, 2009.
17. Dawe JL, Seah CK. Out-of-plane resistance of concrete masonry infilled panels. Canadian Journal of Civil Engineering. 1989 Dec 1;16(6):854-64.
18. D'Ambrisi A, Feo L, Focacci F. Experimental and analytical investigation on bond between Carbon-FRCM materials and masonry. *Composites Part B: Engineering*. 2013; 46: 15-20.
19. Dehghani A, Fischer G. and Nateghi AF Strengthening masonry infill panels using engineered cementitious composites. *Materials and Structures*, 2015; 48:185–204
20. Deng, M, and Yang, S. Cyclic testing of unreinforced masonry walls retrofitted with engineered cementitious composites. *Construction and Building Materials*, 2018; 177: 395–408.
21. European Committee for Standardization (CEN). Design of masonry structures-Part 1-1: General rules for reinforced and unreinforced masonry structures, Eurocode 6, Brussels, Belgium, 2005.
22. Federal Emergency Management Agency (FEMA). Evaluation of earthquake damaged concrete and masonry wall buildings: Basic procedures manual, FEMA 306, Applied Technology Council (ATC-43 Project), Washington, D.C., 1998.
23. Federal Emergency Management Agency (FEMA). Prestandard and commentary for the seismic rehabilitation of buildings, FEMA 356, prepared by American Society of Civil Engineers ASCE, Federal Emergency Management Agency, Washington D.C., 2000.
24. Flanagan, RD, and Bennett, RM. Bidirectional behavior of structural clay tile infilled frames. *Journal of Structural*

Engineering, 1999; 125(3): 236-244.
25. Gattesco N, Boem IN, Dudine A. Diagonal compression tests on masonry walls strengthened with a GFRP mesh reinforced mortar coating. Bulletin of Earthquake Engineering. 2015; 13:1703-26.
26. Giaretton M, Dizhur D, Garbin E, Ingham JM, Da Porto F. In-plane strengthening of clay brick and block masonry walls using textile-reinforced mortar. *Journal of Composites for Construction*. 2018;22(5):04018028.
27. Japan Society of Civil Engineers. Recommendations for Design and Construction of High Performance Fiber Reinforced Cement Composites with Multiple Fine Cracks (HPFRCC). Concrete Engineering Series 2008; 82.
28. Komaraneni, S, Rai, DC, and Singhal, V. Seismic behavior of framed masonry panels with prior damage when subjected to out-of-plane loading. *Earthquake Spectra*, 2011; 27(4): 1077-1103.
29. Koutromanos, I, Kyriakides, M, Stavridis, A, Billington, S, & Shing, PB. Shake-Table Tests of a 3-Story Masonry-Infilled RC Frame Retrofitted with Composite Materials. *Journal of Structural Engineering*, 2013; 139(8): 1340–1351.
30. Kumar, S, Rai, DC. Enhancing Flexural Strength of Unreinforced Masonry Members Using Cementitious Matrix-Based Composites, 2022; 125–142, Singapore: Springer.
31. Kumar S and Rai DC. Development of engineered cementitious composite with moderate tensile properties using polyester fibers. *Construction and building materials*, 2023;404.
32. Kumar S and Rai DC. Experimental and numerical studies on the behavior of scaled masonry prism and beams strengthened with ECC. *Journal of Materials in Civil Engineering*, 2024;36 (4).
33. Li VC. From micromechanics to structural engineering – the design of cementitious composites for civil engineering applications. JSCE, *J Struct Mech Earthquake Eng*. 1993;10 (2): 37–48.
34. Li Y., Zhu J. and Wang Z. Investigation on Mechanical Properties of Masonry Infill Wall Strengthened with ECC. *KSCE Journal of Civil Engineering*, 2019; 23:295–306
35. Lin, Y.W., Wotherspoon, L., Scott, A., Ingham, J.MIn-plane strengthening of clay brick unreinforced masonry wallettes using ECC shotcrete, *Eng Struct.,* 2014; 66:57–65.
36. Masonry Standards Joint Committee (MSJC). Building code requirements for masonry structures. TMS 402-11/ACI 530-11/ASCE 5-11, The Masonry Institute, Boulder, American Concrete Institute, ASCE, Farmington Hills, MI, R, VA, 2011.
37. Moon FL, Yi T, Leon RT, Kahn LF. Testing of a full-scale unreinforced masonry building following seismic strengthening. *Journal of Structural Engineering*. 2007 Sep;133(9):1215-26.
38. Oliveira DV, Basilio I, Lourenço PB. Experimental bond behavior of FRP sheets glued on brick masonry. Journal of Composites for Construction. 2011 Feb;15(1):32-41.
39. Papanicolaou CG, Triantafillou TC, Papathanasiou M, Karlos K. Textile reinforced mortar (TRM) versus FRP as strengthening material of URM walls: out-of-plane cyclic loading. *Materials and structures*. 2008 Jan;41:143-57.
40. Priestley, MJN, Calvi, GM, and Kowalsky, MJ. Displacement- based seismic design of structures, Istituto Universitario di Studi Superiori (IUSS), Pavia, Italy, 2007.
41. Prota A, Marcari G, Fabbrocino G, Manfredi G, Aldea C. Experimental in-plane behavior of tuff masonry strengthened with cementitious matrix–grid composites. Journal of Composites for Construction. 2006 Jun;10(3):223-33.
42. Sagar SL, Singhal V, Rai DC, Gudur P. Diagonal shear and out-of-plane flexural strength of fabric-reinforced cementitious matrix–strengthened masonry walletes. *Journal of Composites for Construction.* 2017; 21(4) :04017016.
43. Sagar SL, Singhal V, Rai DC. In-plane and out-of-plane behavior of masonry-infilled RC frames strengthened with fabric-reinforced cementitious matrix. *Journal of composites for construction*. 2019; 23(1): 04018073.
44. Singhal, V, and Rai, DC. Role of toothing on in-plane and out-of-plane behavior of confined masonry walls. *Journal of Structural Engineering*, 2014; 140(9): 04014053.
45. Sinha, P, and Rai, DC. Development and performance of single-axis shake table for earthquake simulation. *Current Science*, 2009; 96(12): 1611-1620.
46. Tassios, TP. Modelling of structures subjected to seismic loading. Small Scale Modelling of Concrete Structures, F.A. Noor and L.F. Boswell, eds., Elsevier Applied Science, New York, 1992; 229-271.
47. Tomaževič, M, and Klemenc, I. Seismic behavior of confined masonry walls. *Earthquake Engineering and Structural Dynamics*, 1997a; 26(10): 1059–1071.
48. Tomaževič, M. Earthquake-resistant design of masonry buildings, Imperial College Press, London, 1999.
49. Tomaževič, M., Klemenc, I, and Weiss, P. Seismic upgrading of old masonry buildings by seismic isolation and CFRP laminates: A shaking-table study of reduced scale models. *Bull. Earthquake Eng*., 2009; 7 (1): 293–321.
50. Yu KQ, Wang YC, Yu JT , Xu SL A strain-hardening cementitious composites with the tensile capacity up to 8%. *Constr. Build. Mater.* 2017;137: 410–419.
51. Zhang ZG, Ma H. , Qian SZ. Investigation on properties of ECC incorporating crumb rubber of different sizes. *J. Adv. Concr. Technol*. 2015; 31 (5): 24.

Statements & Declarations

Funding

The authors declare that no funds, grants, or other support were received during the preparation of this manuscript.

Competing Interests

The authors have no relevant financial or non-financial interests to disclose.

Author Contributions

Subodh Kumar: Conceptualization, Methodology, Experimental work, Formal analysis, Data curation, Writing original draft

Rajat Avasthi: Experimental work, Formal analysis, writing- review & editing

Durgesh C. Rai: Funding acquisition, writing- review & editing, Supervision

Data Availability

The datasets generated during and/or analyzed during the current study are available from the corresponding author on reasonable request.